Materials Advances

ROYAL SOCIETY OF CHEMISTRY

PAPER

View Article Online
View Journal | View Issue



Cite this: *Mater. Adv.*, 2026, 7, 5147

# Sustainable hydrothermal synthesis of ultrasmall carbon quantum dots from drinking coffee and their impact on optoelectronic properties of the methyl cellulose biopolymer

Hawkar A. Mohammed,[a] Sulaiman Y. M. Alfaifi,[b] Dara M. Aziz,[c] Govar H. Hamasalih,[d] Bakhet A. Alqurashy,[e] Shujahadeen B. Aziz *[d] and Sambasivam Sangaraju *[f]

Green synthesis of carbon quantum dots (CQDs) from sustainable precursors offers a promising route toward environmentally friendly optoelectronic materials. In this work, waste coffee-derived CQDs were synthesized *via* a benign, water-based hydrothermal process without toxic reagents and successfully incorporated into a biodegradable methyl cellulose (MC) matrix to engineer polymer nanocomposites with tunable optical properties. The CQDs exhibit a quasi-spherical morphology with abundant surface functional groups, enabling strong interfacial interactions with the MC chains. As a result, significant modulation of the polymer's electronic structure is achieved, evidenced by a pronounced reduction in the optical band gap from 6.1 to 1.9 eV. This behavior is attributed to the formation of localized electronic states and enhanced optically inferred interfacial electronic interactions within the MC/CQD system. Concurrently, the refractive index increases from 1.15 to 1.51, indicating improved polarizability and charge carrier density. The nanocomposites also exhibit modified light propagation characteristics, including reduced group velocity, highlighting their potential in photonic applications. By integrating biomass waste valorization with biodegradable polymer engineering, this study establishes a sustainable and scalable platform for next-generation optoelectronic materials.

Received 7th February 2026,
Accepted 10th April 2026

DOI: 10.1039/d6ma00178e

rsc.li/materials-advances



## 1. Introduction

Carbon-based materials, distinguished by their remarkable versatility and environmentally beneficial qualities, mark a turning point in materials research.[1] The essential physicochemical properties of carbon based materials – ranging from nanodiamonds and carbon nanotubes to graphene and fullerenes – have catalyzed widespread investigation into their diverse industrial and biomedical applications. Among these, carbon quantum dots (CQDs) are a developing class of zero-dimensional nanostructures characterized by their separate quasi-spherical morphology and ultrafine particle size characteristically below 10 nm. Owing to their vigorous fluorescence and tunable optoelectronic properties, CQDs have become a focal point of multidisciplinary research. Their utility spans a broad spectrum of advanced technologies, including high-resolution bioimaging, precision biosensing, and targeted drug delivery systems. Furthermore, their catalytic and electronic efficiencies have led to significant advancements in photocatalysis, photovoltaics, and the development of next-generation optoelectronic devices such as light-emitting diodes (LEDs) and high-sensitivity sensors.[2–4] Initial carbon dot (CD) synthesis employed top-down methodologies, in which graphite was subjected to extensive processing with aggressive chemicals to convert it into graphite oxide, which was then reduced to nano-sized CDs. Bottom-up synthesis techniques, in which smaller molecules polymerize and carbonize to form CDs, are increasingly appealing for their simplicity and versatility. Recently, increasing emphasis has been placed on sustainable synthesis strategies, where biomass-derived precursors such as waste coffee are utilized to produce CQDs *via* environmentally benign processes,

[a] *Department of Physics, College of Science, Charmo University, Chamchamal, Sulaimanyah, 46001, Iraq*
[b] *Chemistry Department, Faculty of Science, King Abdulaziz University, Jeddah, Saudi Arabia*
[c] *Department of Chemistry, College of Science, University of Raparin, Ranya 46012, Iraq*
[d] *Turning Trash to Treasure Laboratory (TTTL), Research and Development Center, University of Sulaimani, Sulaymaniyah 46001, Iraq. E-mail: shujahadeenaziz@gmail.com*
[e] *Department of Chemistry, Faculty of Science, Taibah University, Madina, Saudi Arabia*
[f] *National Water and Energy Center, United Arab Emirates University, Al Ain 15551, United Arab Emirates. E-mail: s_sambasivam@uaeu.ac.ae*

supporting circular economy concepts and green materials development.[5]

Recent initiatives utilize renewable raw materials (*e.g.*, plants) or renewable refined chemicals (*e.g.*, citric acid and amino acids) for the synthesis of CDs.[6] The fabrication of CDs from naturally occurring precursors, particularly plant-based materials, has gained significant importance due to their broad applicability in biomedical technologies and electronic devices. In addition, deriving CDs from renewable sources contributes to environmental protection by offering sustainable pathways for pollution control and waste valorization. A wide range of natural materials, including fruits, vegetables, coffee grounds, tea residues, agricultural waste, sediments, and other organic byproducts, serve as abundant carbon-rich precursors for CD synthesis. Consequently, these green synthesis strategies are increasingly preferred because they are environmentally benign, economically viable, and more sustainable than conventional chemical or physical fabrication methods.[7]

CQDs exhibit a range of attractive properties, such as facile and scalable synthesis routes, high aqueous dispersibility, outstanding photostability, strong photoresponsive behavior, low cytotoxicity, and ease of surface modification. In addition, CQDs demonstrate notable promising catalytic and tunable excitation emission characteristics, making them highly versatile for numerous technological and biomedical applications.[3] These zero-dimensional dots possess a core–shell structure, in which the core, typically measuring 2–3 nm with a lattice spacing of 0.2 nm, may be either graphitic ($sp^2$) or amorphous (a combination of $sp^2$ and $sp^3$ hybridizations). The core is encased in a self-passivating shell composed of several functional groups, including hydroxyl (–OH), carbonyl (C═O), carboxyl (–COOH), and amine ($–NH_2$) groups, which enhance the surface chemistry and optical characteristics of the CQDs. The structural development of CQDs is affected by various parameters, including the precursor type, synthesis process, and parameters like pH, solvent, and length of synthesis.[4,8,9] Furthermore, the CQDs demonstrate notable physicochemical features, including robust photoluminescence and exceptional stability, while providing distinct advantages such as high biocompatibility and straightforward, economical synthesis methods. The photoluminescence behavior of CQDs is strongly governed by the nature of the functional groups present on their surface. Electron-withdrawing functionalities such as carboxyl (–COOH) groups can modulate fluorescence intensity by influencing charge transfer processes, while electron-donating amine ($–NH_2$) groups are capable of shifting emission characteristics through alterations in the electronic structure. In addition to their optical role, these surface functionalities dictate the net surface charge of CQDs: carboxyl groups typically induce a negative charge, whereas amine groups impart a positive charge. This variation in surface charge plays a crucial role in determining colloidal stability as well as electrostatic interactions with surrounding biomolecules.[9]

CQDs can be manufactured from several sources and combined with polymers to produce nanocomposites (NNCs). The advancement of superior CQD/NNC materials through ligand exchange, grafting, and capping enhances the biocompatibility and optoelectrical properties, which is an emerging area of research.[4] Ali *et al.*[9] reported that CODs synthesized from natural dye extracted from hybrid poplar significantly enhanced the optical potential of a PVA matrix, reducing the direct bandgap from 6.35 to 2.87 eV and the indirect bandgap from 5.85 to 2.50 eV. Natural dyes are inherently rich in carbon, oxygen, and other heteroatoms, making them excellent precursors for carbon quantum dot synthesis.

Building on this knowledge, the current work introduces a sustainable and environmentally benign strategy for fabricating highly luminescent CQDs from coffee through a one-step solvothermal process. Methyl cellulose, a semi-synthetic cellulose derivative, was selected as the host biopolymer due to its biodegradability, renewability, and favorable physicochemical characteristics. MC exhibits a relatively high $T_g$ (184–200 °C), good film-forming ability, non-toxic nature, low cost, and good water solubility, along with strong chemical compatibility toward various dopants. Furthermore, the predominantly amorphous structure of MC, combined with its abundance of functional groups, particularly OH and methoxy moieties, promotes strong intermolecular interactions with organic species. These interactions facilitate the uniform incorporation of CQDs, resulting in composite films with improved structural integrity and enhanced optical potential.[10] Recently, numerous fillers have been employed to reduce the optical band gap ($E_{Opg}$) of metal chalcogenides, nanoparticles, dyes, salts, and blends, including copper monosulfide (CuS) nanoparticles,[10] $TiO_2$ nanoparticles,[11] hollyhock (HH) dye,[12] copper chloride ($CuCl_2$),[13] chitosan (CS), methylcellulose (MC),[14] and Ag nanoparticles.[15] The above approaches are based on metal based or dye doped polymers, while in the current project a fully environmentally friendly method has been carried out to obtain polymer composites with a declined optical band gap. To attain a tunable optical response in methylcellulose (MC) matrices, CQDs were created from discarded coffee grounds using a green hydrothermal methodology and added in various volumetric concentrations. The incorporation of these CQDs led to a dramatic improvement of the refractive index to 1.516, compared to 1.159 for pure MC, although the bandgap was reduced to 1.9 eV. The observed bandgap lessening is principally driven by the introduction of localized states and the chemical interaction – specifically hydrogen bonding – between the hydroxyl and carboxyl groups of the CQDs and the MC backbone. These findings suggest that coffee-derived CQDs are operative agents for engineering light–matter interactions in biopolymers, proposing a sustainable alternative for optoelectronic device fabrication.

## 2. Materials and methodology

### 2.1. Materials

Commercial instant coffee powder was used as the carbon precursor for the synthesis of carbon quantum dots, while analytical-grade MC was utilized as the polymer matrix for film

formation. Analytical grade chloroform was utilized for purification. Deionized water was utilized in all studies. All compounds were utilized as obtained without additional purification.

### 2.2. Synthesis of carbon quantum dots

In a typical synthesis, 25 g of finely ground coffee was dispersed in 150 mL of deionized water and stirred magnetically for 25 min under ambient conditions to ensure complete homogenization. The obtained suspension was subsequently sealed in a Teflon-lined stainless-steel autoclave and processed under hydrothermal conditions at 180 °C for 24 hours. Upon completion of the reaction, the autoclave was left to cool naturally to room temperature before further processing. The obtained dark brown solution was initially filtered to remove large particulates and unreacted residues, followed by microfiltration to eliminate remaining suspended impurities. For further purification and removal of uncarbonized organic molecules, the aqueous CQD solution was transferred to a separating funnel and extracted with chloroform. The organic phase (chloroform) containing uncarbonized species was discarded, while the purified aqueous phase containing CQDs was collected for further use. Finally, the CQD solution was stored at 4 °C for subsequent film preparation. The overall synthesis process is illustrated in Scheme 1a.

### 2.3. Preparation and design of methyl cellulose/CQD nanocomposite films

A methyl cellulose solution was prepared by dissolving 1.5 g of MC in 150 mL of deionized water under continuous magnetic stirring until a clear and homogeneous solution was obtained. The resulting solution was subsequently divided into three equal portions of 50 mL each. To fabricate MC/CQD nanocomposite films with varying CQD loadings, predetermined volumes of the prepared aqueous CQD solution were added to MC solutions. No CQD solution was added to the first portion, which served as the pristine MC sample. For the second and third portions, 10 mL and 20 mL of the CQD solution were added, respectively, and then each mixture was stirred thoroughly to ensure uniform dispersion of CQDs within the polymer matrix. Finally, the homogeneous solutions were cast onto clean, level glass substrates using the solvent-casting technique, as shown in Scheme 1b. The films were allowed to dry under ambient conditions until complete solvent evaporation was achieved, yielding smooth, flexible, and free-standing films. The dried films were carefully peeled from the substrates and stored in a desiccator prior to characterization. For clarity, the prepared films were designated according to their CQD content as follows: MCQDS0 (pure MC), MCQDS1 (MC with 10 mL of CQDs), and MCQDS2 (MC with 20 mL of CQDs).

### 2.4. Characterization techniques

The structural, morphological, chemical, and optical properties of the synthesized CQDs and the MC/CQD nanocomposite films were thoroughly examined utilizing a range of complementary characterization techniques. The crystallographic characteristics and structural ordering of the CQDs were

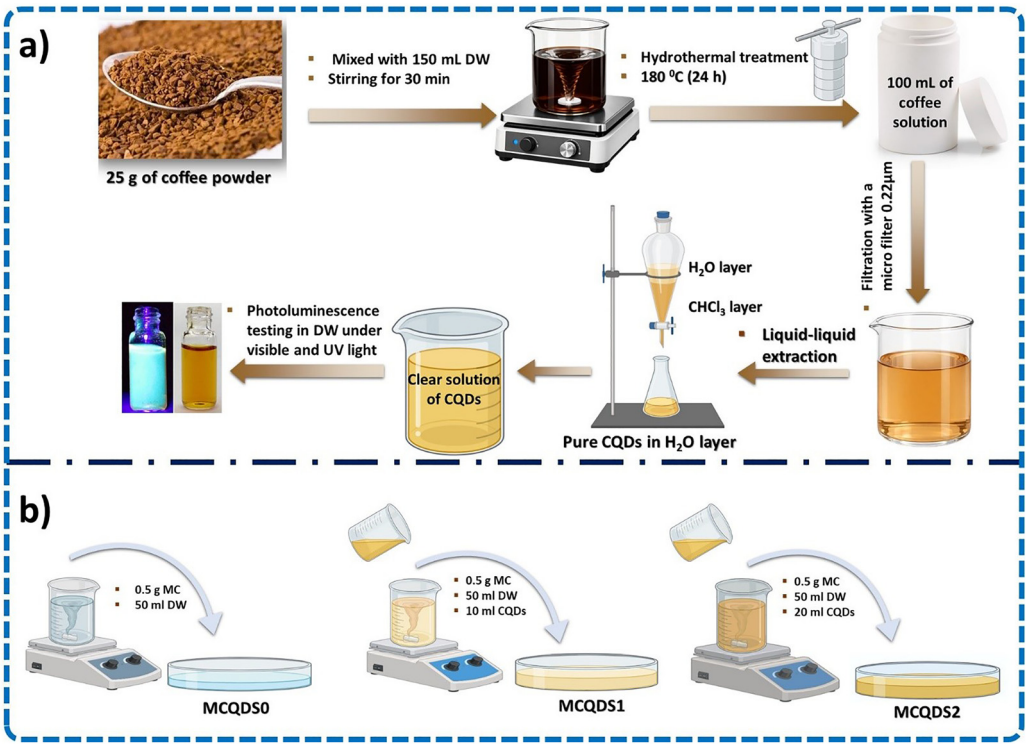


Scheme 1 The key fabrication processes: (a) the hydrothermal synthesis of CQDs derived from drinking coffee and (b) the solvent-casting technique to fabricate MC/CQD nanocomposites.

examined *via* X-ray diffraction (XRD) utilizing an Angstrom Advance ADX 2700 diffractometer with Cu Kα radiation ($\lambda$ = 1.5406 Å), working within a $2\theta$ range of 10–80° and a step increase of 0.1°. The morphology, particle size distribution, and lattice characteristics of the CQDs were analyzed *via* transmission electron microscopy (TEM) and high-resolution transmission electron microscopy (HRTEM) utilizing an FEI Tecnai G2 F30 microscope. FTIR spectra were recorded using an ATR-FTIR spectrometer (Nicolet iS10, Thermo Fisher Scientific) in the wavenumber range of 4000–400 $cm^{-1}$. The spectra were collected at room temperature with a resolution of 4 $cm^{-1}$ and averaged over multiple scans to improve the signal-to-noise ratio. The spectral analysis was performed based on standard vibrational band assignments and comparative evaluation of the peak position, intensity, and band broadening to identify intermolecular interactions between CQDs and the MC matrix. In addition, X-ray photoelectron spectroscopy (XPS) was utilized to determine the elemental composition and chemical bonding states of the CQDs, with measurements carried out using a Thermo Fisher ESCALAB 250Xi system. Optical properties were analyzed using a UV 6100 double-beam spectrophotometer (190–1100 nm) to record the absorbance and transmittance spectra of the films, while photoluminescence (PL) spectroscopy using a Cary Eclipse fluorescence spectrophotometer (Agilent Technologies, USA) was employed to evaluate the excitation-dependent emission behavior of the CQDs. The optical constants, including the absorption coefficient, refractive index, extinction coefficient, dielectric parameters, and optical band gap, were calculated from the UV-vis data using established optical models and theoretical approaches.

# 3. Outcomes and interpretation

## 3.1. XRD

The crystallographic features and structural ordering of the carbon quantum dots produced from coffee powder through a hydrothermal synthesis route were investigated by X-ray diffraction (XRD), with the corresponding diffraction profile presented in Fig. 1. The XRD profile displays two broad diffraction features centered at $2\theta$ = 22.67° and $2\theta$ = 44.15°, which are characteristic of carbon-based nanostructures. The diffraction peak at $2\theta$ = 22.67° corresponds to the (002) plane, while the peak at $2\theta$ = 44.15° is assigned to the (100) plane of carbonaceous materials.[17] Such reflections are characteristic of carbon quantum dots and disordered graphitic carbon derived from biomass precursors. Peak profile fitting indicates that the full width at half maximum of the (002) reflection is 12.05°, whereas the (100) reflection shows a substantially broader FWHM of 41.50°. The pronounced peak broadening, particularly for the (100) plane, indicates an extremely small crystallite size and a high degree of structural disorder, which are hallmarks of nanoscale carbon dots. Such large FWHM values confirm that the synthesized CQDs possess a predominantly amorphous to turbostratic carbon structure, rather than well-ordered crystalline graphite. The (002) diffraction peak

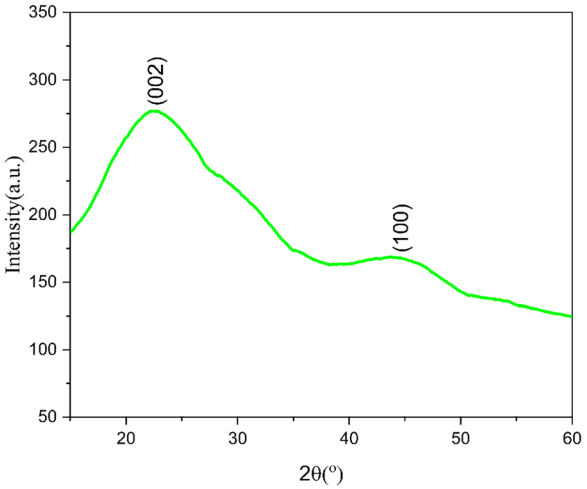


Fig. 1 XRD spectrum of synthesised CQDs.

corresponds to the stacking of graphene-like layers along the *c*-axis. Using Bragg's law, the interlayer spacing corresponding to this reflection is calculated to be approximately 0.38 nm, which is larger than the typical interlayer spacing of bulk graphite (~0.34 nm). This lattice expansion is attributed to the disordered arrangement of carbon layers, the presence of oxygen-containing functional groups, and the ultrasmall size of the CQDs, all of which disrupt regular graphitic stacking (JCPDS No. 26-1076).[16,17] The remarkably broad (100) diffraction peak indicates a lack of long-range in-plane ordering, a hallmark of a turbostratic carbon framework. In this structure, graphene layers are arbitrarily oriented, keeping only short-range order – a common feature of CQDs derived from hydrothermal carbonization. Markedly, the absence of sharp peaks suggests that the product is free from crystalline impurities or residual organic phases. This shows that the chloroform extraction successfully detached unreacted molecules and low-molecular-weight byproducts, leaving behind highly purified carbon nanostructures.

## 3.2. HRTEM

The microscopic characteristics of the synthesized CQDs were investigated using TEM and high-resolution TEM (HRTEM), as shown in Fig. 2. The low-magnification TEM image (Fig. 2a) reveals that the CQDs are predominantly quasi-spherical in morphology and homogeneously dispersed over the examined area, with no evidence of severe agglomeration or particle fusion. This uniform dispersion is attributed to the hydrothermal synthesis route and the subsequent chloroform extraction process, which effectively removes residual organic species and prevents secondary carbon growth and particle aggregation. The absence of large clusters indicates that surface functional groups introduced during hydrothermal carbonization provide sufficient electrostatic and steric stabilization, maintaining the colloidal stability of the CQDs. The statistical analysis of the particle sizes obtained from multiple TEM images (Fig. 2b) shows a narrow size distribution ranging from approximately

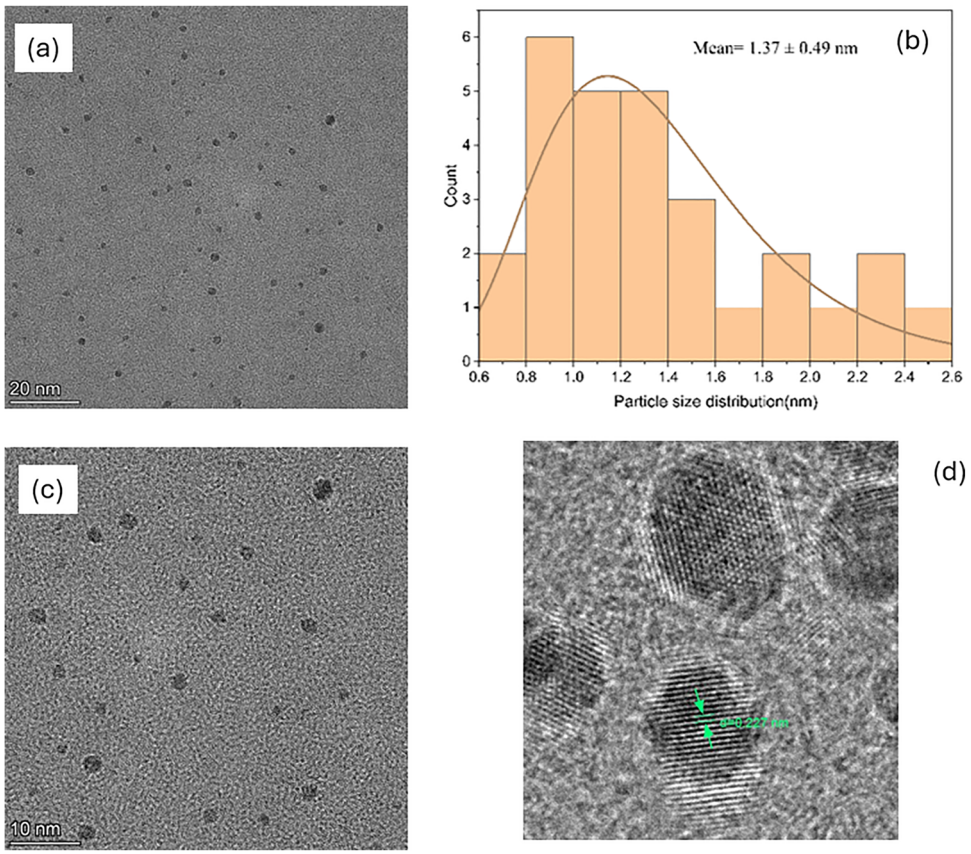


Fig. 2 TEM and HRTEM images of the synthesized carbon quantum dots: (a) low-magnification TEM image, (b) particle size distribution histogram, (c) TEM image, and (d) HRTEM image showing lattice fringes.

0.6 to 2.6 nm, with an average particle diameter of 1.37 ± 0.49 nm. The ultrasmall particle size confirms the formation of true quantum-sized carbon dots. It suggests that nucleation dominates over growth during synthesis, a behavior commonly observed in biomass-derived CQDs synthesized under controlled hydrothermal conditions. The reduced particle size compared to many reported CQDs can also be attributed to the efficient purification of the aqueous CQD solution by chloroform extraction, which limits post-synthesis carbon deposition and aggregation. High-resolution TEM analysis (Fig. 2d) reveals distinct and well-resolved lattice fringes within individual CQDs, confirming the presence of locally ordered graphitic domains embedded in an amorphous carbon matrix. The measured interplanar spacing of approximately 0.227 nm corresponds to the (100) crystallographic plane of graphitic carbon, which is consistent with previously reported values for graphene-like carbon quantum dots derived from green and biomass-based precursors.[18]

The coexistence of ordered lattice fringes and surrounding disordered regions indicates a turbostratic carbon structure characterized by short-range crystallinity and the absence of long-range periodic order, in good agreement with the broad diffraction peaks observed in the XRD analysis. The formation of these graphitic domains arises from localized rearrangement of $sp^2$-hybridized carbon atoms during hydrothermal carbonization of the coffee-derived organic precursors. At the same time, rapid nucleation, heteroatom incorporation, and surface functionalization hinder the formation of extended crystalline lattices, making this structural configuration particularly favorable for quantum confinement and defect-related electronic states, which play a critical role in governing the optical and electronic properties of CQDs.

### 3.3. Fourier transform infrared (FTIR) studies

The surface chemistry and functional group composition of the synthesized CQDs were examined by FTIR, with the resulting spectrum presented in Fig. 3. The FTIR profile indicates the existence of various oxygen and nitrogen-containing functional groups on the CQD surface, a typical characteristic of carbon dots produced from biomass-based precursors. A broad absorption feature observed around 3264 $cm^{-1}$ is attributed to O–H and/or N–H stretching vibrations, confirming the presence of hydroxyl and amine groups generated during the hydrothermal conversion of coffee-derived organic constituents.[19] The broad nature of this band suggests extensive hydrogen bonding among surface functional groups, which contributes to the high aqueous dispersibility and colloidal stability of the CQDs. The absorption bands observed at 3007, 2928, and 2865 $cm^{-1}$ are attributed to the asymmetric and symmetric stretching vibrations of aliphatic C–H bonds, confirming the presence of residual hydrocarbon fragments and partially carbonized organic moieties on the CQD surface.[20]

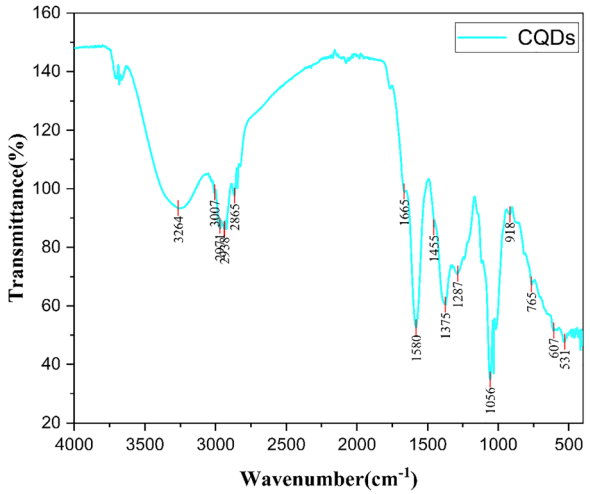


Fig. 3 FTIR spectrum of CQDs prepared from hydrothermal carbonization of drinking coffee.

A prominent absorption band at 1665 $cm^{-1}$ is assigned to the C=O stretching vibration, which may originate from carbonyl or amide groups formed through dehydration and oxidation reactions during hydrothermal treatment. This peak lies within the characteristic range of amide I vibrations (1680–1630 $cm^{-1}$), indicating the possible formation of secondary amide structures on the CQD surface.[20,21] Moreover, the band at 1580 $cm^{-1}$ can be attributed to in-plane N–H bending vibrations or C=C stretching of aromatic $sp^2$ carbon domains, reflecting partial graphitization and nitrogen incorporation within the carbon framework. The absorption peak located at 1455 $cm^{-1}$ is associated with C–H bending vibrations, while the band at 1375 $cm^{-1}$ corresponds to C–N stretching vibrations, further confirming the presence of amine or amide functionalities on the CQDs.[20]

The distinct absorption peak at 1287 $cm^{-1}$ is attributed to C–O stretching vibrations, indicating the presence of alcohol, ester, or ether groups, whereas the strong band at 1056 $cm^{-1}$ is characteristic of C–O–C and C–O stretching modes, commonly observed in oxygen-rich carbon dots derived from plant-based precursors.[19] The weaker bands appearing at 918, 765, 607, and 531 $cm^{-1}$ are assigned to out-of-plane bending vibrations of C–H and C–C bonds and skeletal vibrations of the carbon framework, reflecting the structural complexity and heterogeneity of the CQDs.

Oxygen- and nitrogen-rich surface groups are essential to the CQDs' performance, influencing their surface charge and hydrophilicity. By improving wettability and material compatibility, these functional groups guarantee well spreading and stronger interfacial hold across sensing and bioimaging platforms.[22] FTIR data support this, revealing a hybrid $sp^2/sp^3$ carbon skeleton consistent with eco-friendly synthesis methods.

### 3.4. XPS study

The elemental composition and chemical states of the produced carbon quantum dots were analyzed using X-ray photoelectron spectroscopy (XPS), with the relevant survey and high-resolution spectra displayed in Fig. 4. The broad-scan XPS survey spectrum (Fig. 4a) verifies that the CQDs predominantly consist of carbon, oxygen, and nitrogen, exhibiting distinctive photoelectron peaks at C 1s (~284.8 eV), N 1s (~400 eV), and O 1s (~532 eV), respectively. The quantitative analysis reveals atomic percentages of C 1s = 76.96%, O 1s = 18.7%, and N 1s = 4.35%, indicating that carbon is the dominant element. In contrast, a substantial amount of oxygen and a minor fraction of nitrogen are incorporated into the CQD surface. The presence of oxygen- and nitrogen-containing species originates from the oxygen-rich organic constituents of coffee powder and the nitrogen-based compounds formed during hydrothermal carbonization, confirming successful heteroatom functionalization of the CQDs. Furthermore, the high-resolution C 1s spectrum (Fig. 4b) was deconvoluted into three distinct components, revealing the complex carbon bonding environment within the CQDs. The dominant peak centered at approximately 284.6–284.8 eV is attributed to C–C/C=C bonds, corresponding to $sp^2$- and $sp^3$-hybridized carbon frameworks forming the core structure of the CQDs.[23] The second component, observed at around 285.8–286.2 eV, corresponds to C–N and C–O bonds, indicating the presence of nitrogen- and oxygen-containing functional groups on the CQD surface.[24] Additionally, the higher binding energy peak near 288.3–288.8 eV is attributed to C=O groups, such as carbonyl or carboxyl functionalities, which typically form through oxidation during hydrothermal synthesis.[24] These findings confirm that the CQDs have a mixed $sp^2/sp^3$ carbon framework decorated with polar surface functional groups.

The high-resolution N 1s spectrum (Fig. 4c) further elucidates the chemical state of nitrogen within the CQDs. The spectrum can be fitted into two main components: a prominent peak centered at approximately 399.5–400.2 eV, which is attributed to graphitic (quaternary) nitrogen, and a secondary peak located at around 401.5–402.2 eV, corresponding to pyridinic nitrogen.[25] The graphitic nitrogen is incorporated within the carbon lattice and contributes to enhanced electronic conductivity, while pyridinic nitrogen is typically located at the edges or defects of the carbon framework and plays a crucial role in surface reactivity and charge transfer processes.[26] Furthermore, the presence of these nitrogen configurations confirms successful nitrogen doping of the CQDs during hydrothermal treatment, even without the addition of external nitrogen precursors. The high-resolution O 1s spectrum (Fig. 4d) was deconvoluted into two prominent peaks, further confirming the oxygen-rich surface chemistry of the CQDs, as well as the dominant peak at approximately 532.7–533.2eV, which is attributed to C–O bonds, including hydroxyl and ether groups. The lower binding energy component centered at around 530.8–531.5 eV corresponds to C=O bonds, such as carbonyl and carboxyl functionalities.[24,27] As verified by FTIR analysis, these functional groups indicate that the carbon framework suffered incomplete oxidation during synthesis. The resulting density of oxygen and nitrogen surface groups boosts the CQDs' hydrophilicity and dispersibility. These polar sites enable strong aqueous interactions and thus the CQD particles are ideal for

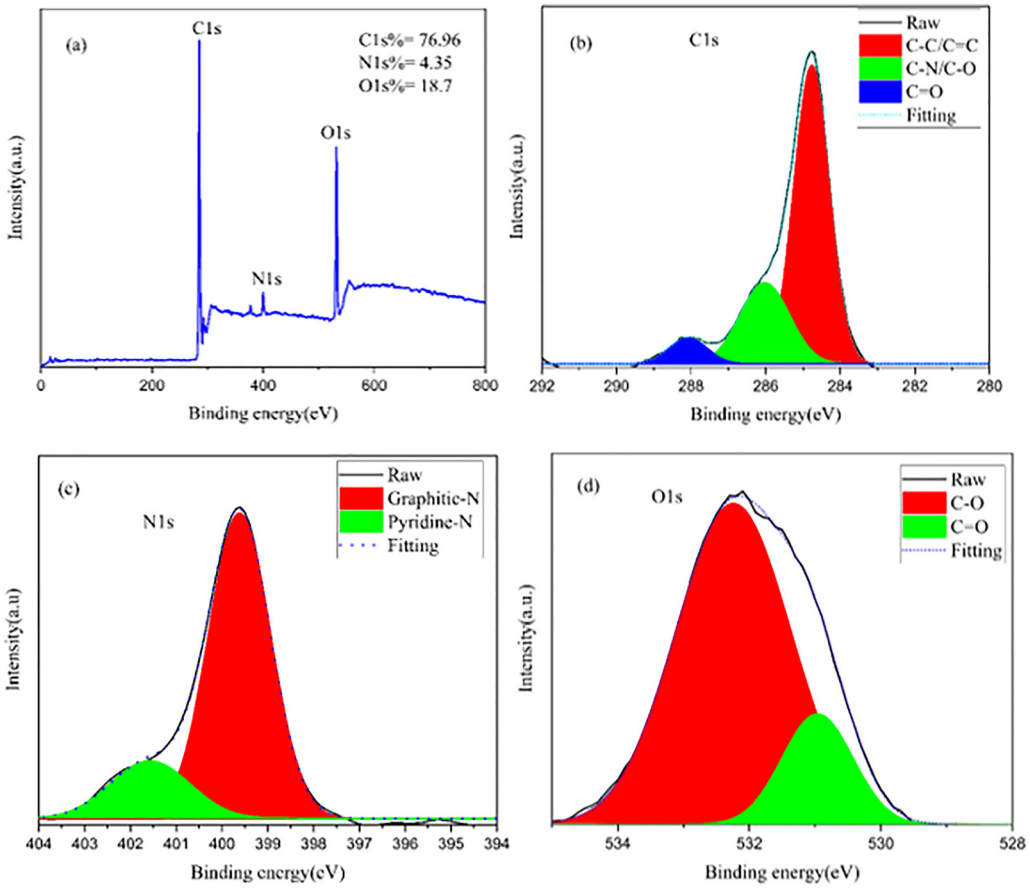


Fig. 4 (a) XPS survey spectra of coffee-derived CQDs and the high-resolution XPS spectra of (b) O1s, (c) N1s, and (d) C1s.

applications ranging from bioimaging to optoelectronic devices.

### 3.5. Photoluminescence spectral analysis

The optical behavior of the prepared carbon quantum dots was comprehensively examined through excitation and photoluminescence (PL) spectroscopic analyses, as illustrated in Fig. 5. The excitation and emission profiles of the CQDs are depicted in Fig. 5a. The excitation spectrum exhibited two prominent bands located at approximately 242 nm and 343 nm when observed at 423 nm. The higher-energy band in the ultraviolet region is ascribed to π–π* electronic transitions within aromatic $sp^2$-hybridized carbon frameworks, while the lower-energy excitation centered near 343 nm is related to n–π*

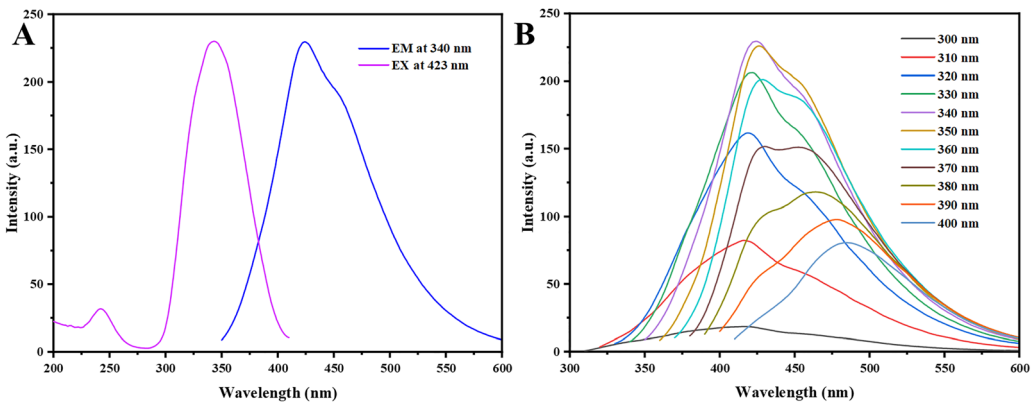


Fig. 5 (A) Excitation and photoluminescence (FL) spectra of the carbon dots (CDs). (B) Photoluminescence emission spectra of the CDs recorded at different excitation wavelengths.

transitions arising from surface defect states and heteroatom-containing functional groups. Hence, these assignments are consistent with the surface chemical features identified by the FTIR and XPS analyses. Upon excitation at 343 nm, the CQDs exhibit a strong blue emission with a maximum centered at 423 nm, confirming the formation of optically active carbon nanodots with well-defined emissive states.

Fig. 5b demonstrates the excitation-dependent photoluminescence response of the CQDs over an excitation wavelength range of 300–400 nm. As the excitation wavelength is shifted from 300 to 340 nm, the emission intensity increases, reaching a maximum at 423 nm. Beyond this excitation wavelength, a gradual attenuation in emission intensity is observed. This excitation-dependent emission behavior is a well-known characteristic of carbon quantum dots. It is generally attributed to the coexistence of multiple emissive surface sites, diverse energy trap states, and non-uniform surface functionalization, all of which introduce localized electronic states within the electronic band structure. Consequently, these results suggest that the photoluminescence of the CQDs arises from the combined effects of quantum confinement and surface-state-dominated radiative recombination. The fluorescence quantum yield (QY) of the CQDs was measured at 4.55%, demonstrating competitive luminescence efficiency compared with several biomass-derived carbon dots reported in the literature using simple and environmentally benign synthesis routes. For instance, CQDs prepared from food waste *via* ultrasonication exhibited a relatively low QY of 2.85%,[28] while CQDs derived from waste frying oil showed a QY of only 3.6% despite the use of acid-assisted heating.[29] Similarly, carbon dots synthesized from willow bark,[30] grass,[31] and pomelo peel[32] typically display quantum yields in the range of 6–7%, often requiring longer reaction times or more energy-intensive hydrothermal processes. In contrast, the CQDs developed in this study exhibit comparable photoluminescence efficiency under relatively mild synthesis conditions, without the use of harsh chemicals or extended processing times. Although higher quantum yields have been reported for CQDs derived from sources such as orange peel[33] or gelatin,[34] those systems typically require prolonged reaction durations or more complex processing strategies, which may limit their scalability and sustainability. Therefore, the optical potential of the CQDs synthesized in this work represents a favorable balance between photoluminescence efficiency, green synthesis, and process simplicity, highlighting their potential for practical applications in fluorescence-based sensing, bioimaging, and optoelectronic devices.

### 3.6. UV-vis study of CQDs

CQDs' UV-vis absorption spectra are essential for understanding their surface chemistry and electrical structure, so because of their nanoscale size and the existence of different chemical functional groups, carbon quantum dots show discrete absorption peaks in contrast to bulk carbon, such as graphite. CQDs produced in this work exhibit notable absorption in the ultraviolet range with a tail that extends into the visible spectrum, according to their UV-vis absorption spectra. The absorption spectra of both concentrated and diluted CQDs are shown in Fig. 6. The spectra clearly show two separate absorption bands: a noticeable peak in the 230–270 nm region and a less noticeable shoulder or peak in the 300–350 nm range.[3] A shoulder is observed at about 360 nm, which is related to the n–π* orbital transition associated with the sp3 hybridization, which is indicative of bonds between carbon atoms and functional groups containing nitrogen and oxygen. The first peak is associated with the π–π* transition of the $sp^2$ hybridized carbon framework (C═C bonds).[35] The aromatic C═C bonds inside the $sp^2$ hybridized carbon framework are the origin of π–π* transitions, so this transition is analogous to that observed in graphene or benzene.[36,37] Moreover, aromatic C═C bonds are not static double bonds; instead, they manifest as delocalized pi–electron clouds within cyclic structures, rendering them stronger, shorter (approximately 1.39 Å in benzene), and more stable than conventional alkenic C═C bonds. Breaking these bonds requires considerable energy, such as that provided by metal catalysts or potent oxidants, whereas simple double bonds readily participate in addition reactions. Their distinctive stability arises from aromaticity, as dictated by Hückel's rule.[37] At extended wavelengths, n–π* appears as a shoulder or a diminished peak. This phenomenon is attributed to the presence of non-bonding electrons from heteroatoms, specifically nitrogen in C═N bonds, when the nitrogen is doped, or oxygen in C═O (carbonyl) or COOH (carboxyl) groups. The exact position and intensity of these peaks are highly tunable and depend on surface passivation, synthesis methods, and precursor materials. The optical bandgap can be reduced by doping with heteroatoms such as nitrogen or sulfur, which introduce new energy levels that shift the absorption into the visible spectrum. In samples with high concentrations of CQDs, the absorption shifted to the visible spectrum due to π–π stacking among the CQD sheets. Intense optical absorption in the visible spectrum is typically succeeded by an exponential decline up to 800 nm (red curve) in the UV-vis absorption of CQDs, as shown in Fig. 6. The highest peak is likely attributable to oxidation and imperfections in the π-bonding associated with $sp^2$ carbon hybridization. The presence of $sp^2$ carbon hybridization suggests that the CQD core contains both crystalline and amorphous graphitic domains. Moreover, the absorbance decreases with increasing wavelength, indicating that these nanoparticles possess a defined optical bandgap.[35] For most CQDs, the bandgap lies between 2.0 eV and 4.0 eV, which explains why they are highly active under UV and blue light excitation.

### 3.7. FTIR analysis of MC and MC/CQD nanocomposite films

FTIR spectroscopy was applied to elucidate the chemical structure of pristine methyl cellulose and to investigate the interfacial interactions induced by the incorporation of carbon quantum dots within the MC matrix. The FTIR spectra of (a) pure MC (MCQDS0), (b) MC/CQD film containing 10 mL CQDs (MCQDS1), and (c) MC/CQD film containing 20 mL CQDs (MCQDS2) are presented in Fig. 7.

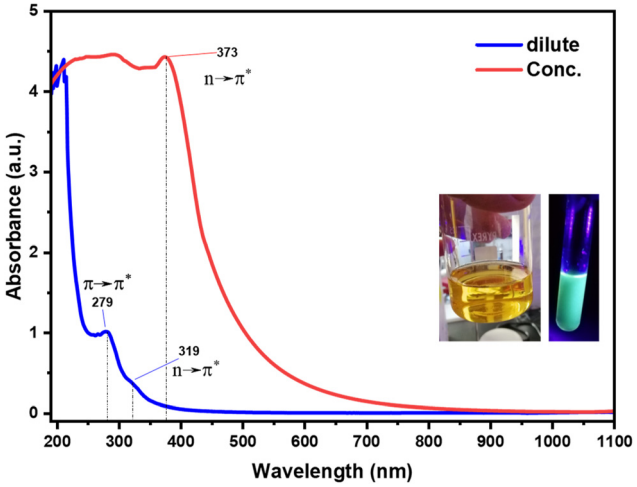


Fig. 6 UV-visible absorption spectra of carbon quantum dots (CQDs) at varying concentrations, revealing how their optical absorption shifts with concentration, and the inset photos display the aqueous CQD solution under normal daylight and UV light, highlighting its distinctive fluorescent glow.

For the pristine MC film (Fig. 7a), a broad absorption band centered at approximately 3440 $cm^{-1}$ is observed, which is characteristic of O–H stretching vibrations arising from hydroxyl groups in the cellulose backbone and hydrogen-bonded water molecules.[38] The bands located at 2984–2835 $cm^{-1}$ correspond to asymmetric and symmetric C–H stretching modes of $–CH_3$ and $–CH_2$ groups associated with the glucopyranose units of MC.[39] A distinct band at 1642 $cm^{-1}$ is attributed to the bending vibration of absorbed water (H–O–H), a common feature in hydrophilic polysaccharides.[40] The peaks at 1455 and 1371 $cm^{-1}$ are assigned to C–H bending and $–CH_3$ deformation vibrations, respectively, while the bands appearing at 1311–1189 $cm^{-1}$ are related to C–O–C stretching and skeletal vibrations of the cellulose ether structure. The strong

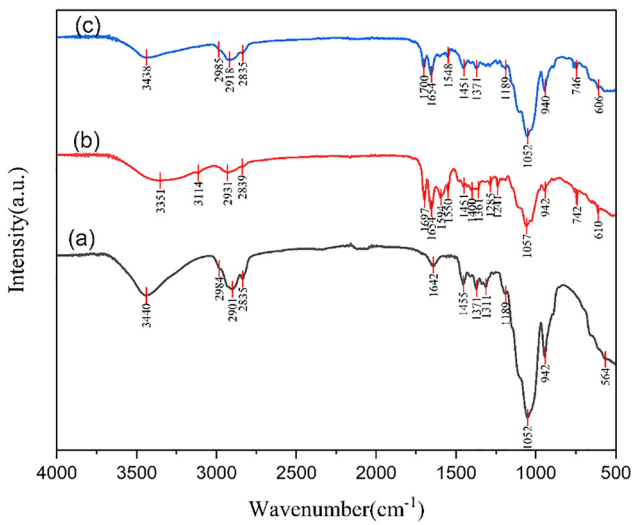


Fig. 7 FTIR spectra of (a) MCQDS0, (b) MCQDS1 and (c) MCQDS2 composite films.

absorption near 1052 $cm^{-1}$ is characteristic of C–O stretching in the pyranose ring, confirming the integrity of the MC backbone, whereas the low-frequency band around 564 $cm^{-1}$ is associated with skeletal vibrations of the polymer chain. Upon incorporation of CQDs into the MC matrix (Fig. 7b and c), noticeable changes in both peak position and intensity are observed, indicating strong interactions between MC chains and CQDs. Therefore, in the MCQDS1 sample (Fig. 7b), the broad O–H stretching band shifts slightly toward lower wavenumbers ($\approx$3351 $cm^{-1}$) and becomes broader, indicating enhanced hydrogen bonding between methylcellulose hydroxyl groups and oxygen- and nitrogen-containing functional groups on the CQD surface. This behavior is further accentuated in the MCQDS2 film (Fig. 7c), where the O–H/N–H stretching band appears at $\approx$3438 $cm^{-1}$, reflecting a modified hydrogen-bonding environment resulting from the higher CQD loading.[41] In addition, new absorption bands emerge or existing bands intensify in the nanocomposite films, particularly in the 1700–1550 $cm^{-1}$ region. Weak features observed at $\approx$1697–1650 $cm^{-1}$ are attributed to C═O stretching vibrations associated with carboxyl and carbonyl groups on the CQD surface. The presence of these bands provides strong evidence for the successful incorporation of CQDs and is consistent with biomass-derived CQDs containing abundant surface functional groups. Moreover, the bands around 1548–1515 $cm^{-1}$ are associated with N–H bending or C═N stretching vibrations, confirming the contribution of nitrogen-containing surface states introduced by CQDs. In the fingerprint region, the characteristic MC peaks at 1052–1057 $cm^{-1}$ remain prominent in all samples, indicating that the polymer backbone remains structurally intact after CQD incorporation. However, slight shifts and intensity variations in the 1050–1200 $cm^{-1}$ range suggest strong interfacial interactions between MC chains and CQDs through hydrogen bonding and dipole–dipole interactions. In addition, the appearance and enhancement of bands near 940–746 $cm^{-1}$ in the nanocomposite films further support changes in the local molecular environment due to CQD–polymer coupling.

### 3.8. Optical properties

**3.8.1. Absorption and transmittance study.** Polymeric systems can absorb incident radiation in the UV-vis zone through electronic excitation processes. During the absorption process, electrons are migrated from their unexcited state to higher-energy excited states. The nature of these electronic transitions is governed by the polymer's intrinsic electronic structure, which is defined by the arrangement of molecular orbitals, including σ orbitals associated with bonding interactions, π orbitals responsible for delocalized bonding, and non-bonding (n) orbitals arising from lone electron pairs. These molecular orbitals originate from the combination of atomic orbitals within the polymer framework. Additionally, structural defects or impurity species are able to initiate localized energy states within the forbidden band structure, enabling distinct optical transitions. When such transitions occur within the visible

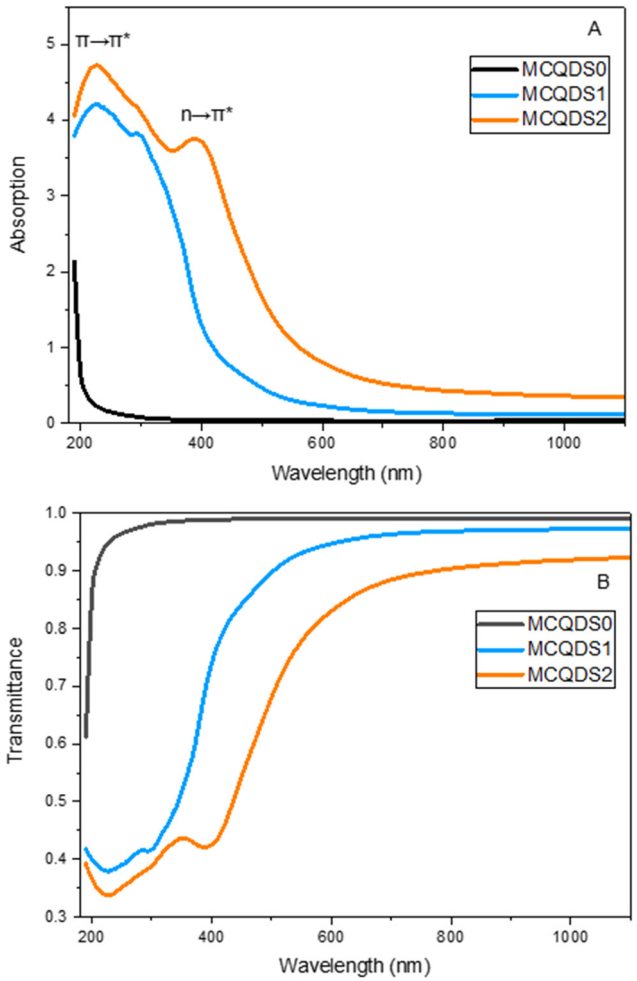


Fig. 8 (A) The absorption and (B) transmittance spectra against the wavelength for pure and MC-doped CQDs.

region, the defect-related states are commonly referred to as color centers.[42]

Absorbance is essential for characterizing CQDs for various applications. In addition, CQDs generated by different processes display distinct absorption spectra. Fig. 8A displays the UV-vis absorption spectrum of both pristine MC and modified CQDs. The UV-vis spectra of MCQDS0, MCQDS1, and MCQDS2 exhibit the distinctive absorption characteristics of carbon quantum dots, wherein both the core structure and surface functional groups significantly affect the optical response. All samples exhibit a pronounced absorption band in the deep-UV region (~227 nm), which arises from π → π* transitions of aromatic C═C and C═N bonds within the $sp^2$-hybridized carbon domains. A secondary, broader absorption feature is observed at approximately 290 nm for MCQDS1 and shifts to around 388 nm for MCQDS2, corresponding to n → π* transitions associated with surface functional groups such as –OH, –COOH, and C═O moieties.[9,43] The presence of surface functionalities, including –OH, $–NH_2$, –COOH, and –C═O groups, as confirmed by FTIR analysis, promotes n → π* electronic transitions and increases the density of surface-related energy states. These effects collectively account for the progressive redshift toward longer wavelengths. Furthermore, these functional groups enhance the interfacial affinity and interaction between the CQDs and methylcellulose chains, resulting in stronger light absorption in the visible region. This behavior provides clear evidence that the CQDs are effectively incorporated into the MC matrix and actively modulate its optical response through enhanced interfacial bonding and more efficient electronic transitions. From an application perspective, CQDs induce optical properties in the MC matrix, and modifiying its optical behavior is a critical requirement for efficient light harvesting, making such materials attractive for use in solar energy conversion, photodetection systems, and ultraviolet-shielding coatings.[44] Furthermore, pristine MC exhibits near-complete transparency within this wavelength region, as evidenced by the absence of noticeable absorption in the visible range (the black curve in Fig. 8A), which is consistent with its insulating nature. It is well established that optical absorption does not occur when the photon radiation energy is lower than the $E_{Opg}$ between accessible electronic states, so the material remains transparent to the incoming radiation. Once the photon energy exceeds this threshold, absorption becomes possible, enabling electronic transitions from the valence band to higher-energy states.

In contrast, the pronounced absorption observed for the CQDs is attributed to the presence and enhancement of additional electronic states, which are responsible for the increased absorption intensity in the CQD-doped MC samples.[45] The transmittance spectra of pure and doped MC polymers with different concentrations of CQDs are displayed in Fig. 8B. Beyond the visible range, the pure MC showed a relatively high degree of transparency; however, the transmittance decreased when CQDs were added. Because of their surface functional groups and electronic structure, CQDs strongly absorb light, which accounts for the drop in transmittance observed when they are added to the MC polymer. This phenomenon indicates that the additional CQD fillers interact strongly with the functional groups within the MC polymer chains, thereby reducing the transparency of the doped films. By blocking dangerous radiation, protective coatings and optical filters operate better when transmittance in the UV region is reduced.[44]

**3.8.2. Absorption edge and Urbach energy study.** The absorption coefficient (α) of a material significantly influences its selection for potential applications; this signifies its capacity for light absorption.[46] A valuable technique for investigating electronic transitions is UV-visible spectroscopy. The absorption edge in both crystalline and non-crystalline materials can be utilized to ascertain $E_{Opg}$. The region where an incoming photon causes an electron to jump to an upward energy transition is known as the absorption edge.[47] This is known as the percentage of power absorbed per unit length of the medium. The following formula was used to determine the absorption coefficient.[48]

$$\alpha = \left(\frac{2.303A}{t}\right) \quad (1)$$

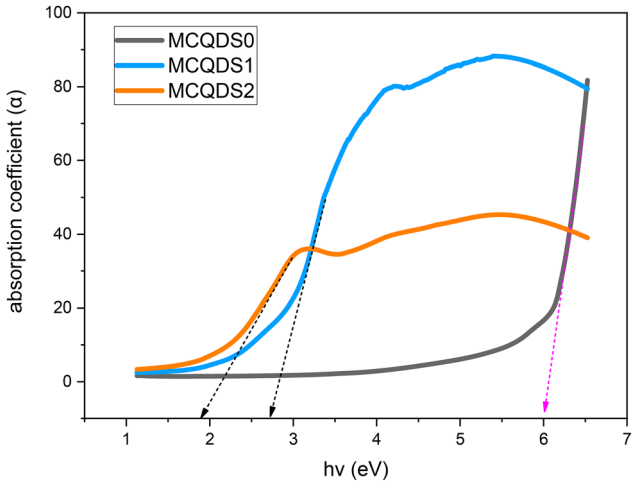


Fig. 9 The absorption edge spectra against incident photon energy ($h\nu$) for pure and MC-doped CQDs.

where $t$ is the sample thickness and $A$ is the absorbance. Fig. 9 displays the $\alpha$ of pure and doped MC films with photon energy ($h\nu$). Extrapolating the linear component of $\alpha$ against applied photon energy curves at the absorption zero value yielded the absorption edge ($E_{edg}$) value.[15] As evident in Table 1, adding CQDs to the MC polymer reduced the $E_{edg}$. According to quantitative measurements, the $E_{edg}$ for pure MC (MCQDS0) is around 6 eV, which drops to 2.75 eV for MCQDS1 and then to 1.9 eV for MCQDS2. It is evident that the $E_{edg}$ moves toward higher wavelengths as the concentration of CQDs rises. Bond cleavage and repair may have created a conjugated bond system, which is what produced the change in the $E_{edg}$. This corroborates the structural and chemical alterations of MC when amalgamated with CQDs.[47] This lowers the photon energies, verifying that the $E_{Opg}$ of the CQDs-doped MC samples is significantly smaller than that of pure MC. The higher Urbach energy ($U_{rb}$) is a reflection of the additional structural disorder and defect states introduced by the insertion of CQDs. These defects facilitate electronic transitions between the valence band (VB) and conduction band (CB) by increasing the density of localized states. The incorporation of CQDs into the MC polymer reduces the absorption edge energy ($E_{edg}$), which can be attributed to heteroatom-rich surface states of the CQDs (–OH, –COOH, and C═O) and their interaction with the functional groups of the MC polymer. These interactions enhance charge-transfer processes, as further evidenced by the progressive decrease in the optical bandgap energy ($E_{Ogp}$) with increasing CQD loading. To further clarify the origin of these optical transitions, the behavior of the MC/CQD nanocomposite can be conceptually described in terms of energy-level interactions. The pristine MC polymer possesses a wide band gap, while the incorporation of CQDs introduces discrete energy levels associated with small graphitic domains. In addition, abundant surface functional groups generate localized defect states within the forbidden gap. These localized states act as intermediate energy levels that facilitate sub-band-gap optical transitions. Consequently, the observed optical absorption and apparent band gap narrowing arises from transitions involving these defect and interfacial states, rather than direct band-to-band transitions as in crystalline semiconductors. CQDs induce optical properties in the MC matrix and modify its optical behavior and stronger light–matter interaction inside the nanocomposite. This makes them potential candidates for optoelectronic device applications.

Table 1 Fluctuation of the absorption edge and Urbach energy parameters in pure and CQD-incorporated MC samples

| Samples | $E_{edg}$ (eV) | $U_{rb}$ (eV) |
|---|---|---|
| MCQDS0 | 6 | 0.2757 |
| MCQDS1 | 2.75 | 0.5299 |
| MCQDS2 | 1.9 | 0.6289 |

The $U_{rb}$ serves as an effective parameter for assessing whether a material exhibits predominantly amorphous or crystalline characteristics following doping. The presence of an Urbach tail is a hallmark of structurally disordered and amorphous systems and provides valuable insight into their electronic transport behavior. In amorphous materials, these band-tail states originate from local structural distortions and network strain, which shift electronic states into the forbidden energy gap. The resulting tail states extend exponentially into the bandgap region. Accordingly, in the low-absorption regime, the absorption coefficient ($\alpha$) follows the Urbach relation.[49]

$$\alpha = \alpha_0 \exp^{\frac{h\nu}{U_{rb}}} \quad (2)$$

In this relation, $\alpha_0$ represents a proportionality constant, while the $U_{rb}$ corresponds to the characteristic width of the localized tail states extending into the forbidden bandgap. The value of $U_{rb}$ can be extracted from the 1/slope of the linear regions obtained in plots of ln($\alpha$) as a function of $h\nu$, as illustrated in Fig. 10. The calculated $U_{rb}$ for pristine MC is 0.2757 eV, whereas a substantially higher value of 0.6289 eV is observed for the CQD-doped MC sample, as summarized in Table 1. This increase in Urbach energy is indicative of an enhanced degree of structural disorder and amorphization within the CQDs/MC nanocomposite network. The broadening of the band-tail states reflects the introduction of imperfections and localized states in the electronic structure of the host matrix.[50] Prasher *et al.* have established that the rise in $U_{rb}$ signifies the augmentation of the amorphous component.[51] Adding functional groups like $-NH_2$, –C═O, –OH, and –COOH to the surface of CQDs is very important. These groups create defect sites that trap energy and interact strongly with the hydroxyl and methoxy groups of MC, which makes the nanocomposite more structurally disordered. The wide diffraction peaks shown in the XRD pattern show that the CQDs that were made have mostly an amorphous to turbostratic carbon structure. The significant peak broadening and small crystallite size show that there is a lot of structural disorder, which means that there is no long-range crystalline ordering. The structural data from XRD match the optical data. The rise in Urbach energy shows that there are more localized states (see Section 4.8.5) that are linked to structural disorder.

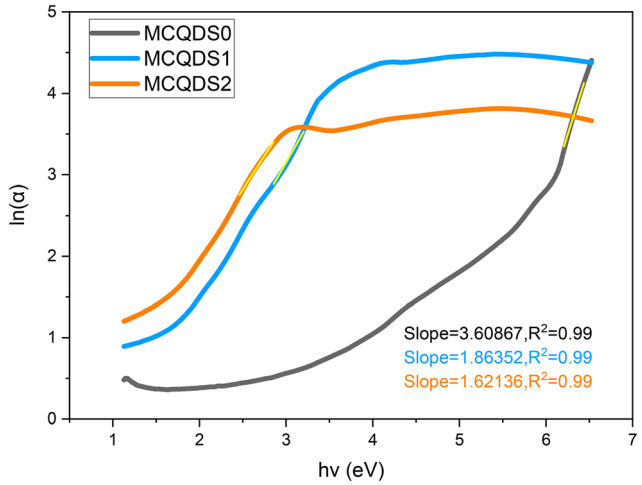


Fig. 10 The ln(α) spectra against $h\nu$ for pure MC and MC/CQD nanocomposite films.

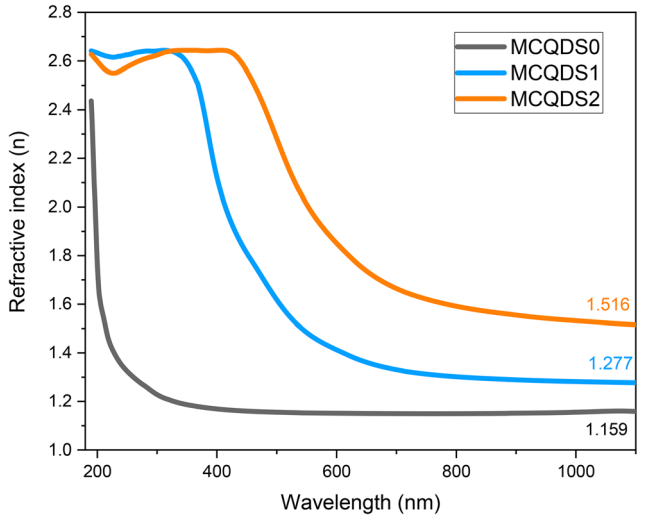


Fig. 11 Index of refraction ($n$) spectra against incident wavelength (nm) for pure MC and MC/CQD nanocomposite samples.

The Urbach energy measurements back up the XRD data, showing that there is a strong link between the CQDs' microstructural qualities and their optical electronic properties.

**3.8.3. Refractive index and extinction coefficient.** The evaluation of optical constants, particularly the refractive index and extinction coefficient, is essential for assessing materials intended for optoelectronic applications. The refractive index is a fundamental intrinsic property that describes how light or electromagnetic radiation propagates through an optical medium. When an incoming radiation beam strikes the contact between two substances possessing dissimilar refractive indices, both its velocity and direction of propagation are altered. In materials that exhibit optical absorption, the refractive index must be expressed as a complex quantity to account for energy loss, thereby enabling an accurate description of the absorptive behavior of the medium[52,53]

$$\tilde{n} = n + ik \tag{3}$$

Let $\tilde{n}$, $n$ and $k$ denote the complex refractive index, the actual refractive index, and the extinction coefficient, respectively. The values of $n$ were derived from the $k$ and reflectance ($R$) by Kramers–Kronig relations.[54]

$$n(\lambda) = \sqrt{\frac{4R}{(1-R)^2} - k^2} + \frac{1+R}{1-R} \tag{4}$$

where $k = \alpha\lambda/4\pi t$, which is inversely related to specimen width ($t$) and directly related to wavelength ($\lambda$) and $\alpha$. The Beer–Lambert law calculates reflectance from absorbance ($A$) and transmittance ($T$), and for transmittance calculations, use $T = 10^{-A}$.[47,55] Fig. 11 illustrates the variation of $n$ with $\lambda$ for both pristine and modified MC samples. The findings indicate that incorporating CQD fillers into the MC polymer altered the refractive index of the films, increasing it from 1.159 to approximately 1.516. When a material is exposed to incoming electromagnetic radiation, its internal charge distribution will experience time-varying forces due to the electric field (EF) component of the incident radiation. The extensive dispersion region is attributed to the samples' polar characteristics. At high wavelengths, polar molecules will be unable to respond to the field oscillation due to their inertia. The refractive index evidently increased with increasing CQD concentration. The refractive index depends on both density and polarizability. Consequently, the augmentation of CQD concentration introduces heteroatom-rich functional groups that generate localized electronic states and facilitate the formation of space charge at the CQD–polymer interfaces. The resulting increase in localized charge density within the band gap enhances the material's electronic polarizability, which in turn contributes to the increase in the refractive index of the NNC. We have shown in prior studies that when the refractive index goes up, the $E_{Opg}$ invariably goes down.[56–58] Polymers exhibiting high refractive indices have recently attracted considerable attention for a wide range of technological applications, including display technologies, next-generation organic light-emitting diodes (OLEDs), anti-reflection coatings, diverse semiconductor-based devices,[59] optical adhesives,[53] and ophthalmic applications.[53]

The extinction coefficient reflects a material's attenuation of incident electromagnetic radiation. Fig. 12 presents the dependence of $k$ on wavelength ($\lambda$). The wavelength-dependent variation of $k$ signifies the interaction between incoming photons and the medium. Physically, the extinction coefficient describes the reduction in the intensity of an electromagnetic wave per unit thickness of the material due to absorption and scattering.[48] The $k$ rises with increasing CQD concentration; however, its growth is minimal in comparison to that of $n$. The low $k$ signifies that the composite samples remain highly clear.[60] In short, adding CQDs to the MC polymer raises the extinction coefficient. This is mostly because the CQDs' conjugated carbon cores, defect states, and surface functional groups enhance the polymer's light absorption. This trend aligns with the observation that the $E_{Opg}$ has decreased and the composite's refractive index has increased.

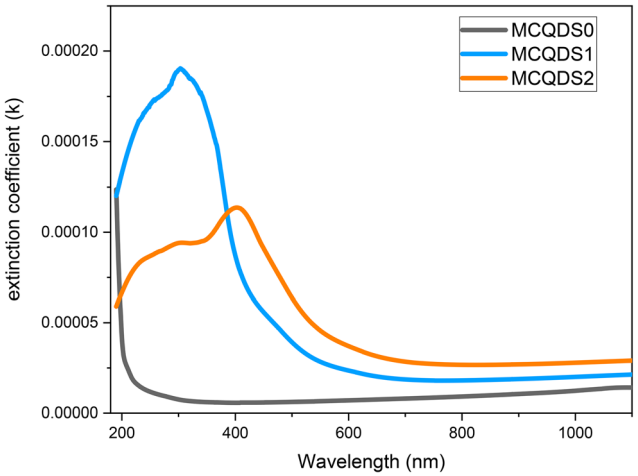


Fig. 12 Extinction coefficient ($k$) spectra against the incident wavelength (nm) for pure MC and MC/CQD nanocomposite samples.

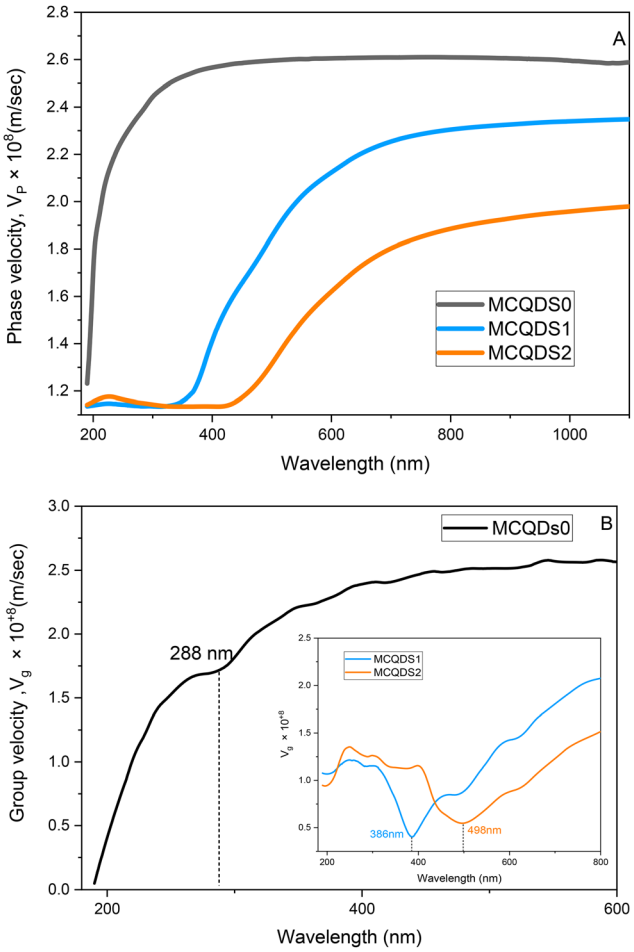


Fig. 13 (A) Phase velocity and (B) group velocity spectra against the wavelength (nm) for pure MC and MC/CQD nanocomposite samples.

**3.8.4. Phase and group velocity.** In optical science, phase velocity $V_P$ and group velocity $V_g$ are the two essential physical parameters of refractive index scattering. In optics, the phase velocity of an electromagnetic wave is the speed at which a particular part of the wave, like its crest or trough, moves through a medium. The value is determined by the material's refractive index and the incident light's wavelength. The phase velocity can be computed analytically as $V_P = c/n$, where $c$ is the light speed. The incorporation of CQDs into the film increases its density, thereby increasing the refractive index, as demonstrated in Fig. 13A. Consequently, the higher refractive index of MC: CQDs leads to slower propagation of light through the material.

The $V_g$ is the rate at which the envelope of an optical oscillation packet propagates across a medium. It quantifies the velocity at which the energy or data are transmitted as a wave packet propagates. The $V_g$ of light in the doped MC material can be altered by dispersion processes induced by additives or dopants like CQDs. The parameter values are computed using the formula depicted in Fig. 13B.[61]

$$V_g = 3 \times 10^8 \Big/ \left(n - \left(\lambda \frac{dn}{d\lambda}\right)\right) \quad (5)$$

In Fig. 13A, $V_P$ performs better than the group velocity, and the combined effect of the two components increases with the wavelength. However, both values decrease as the CQD content increases. This variation may be due to the rise in the $n$ of the compositions as the CQD content rises. The $E_{Opg}$ at each curve's apex correlates with a negative segment of the $dn/d\lambda$ factor.[62] Using $E_{Opg} = 1239.83/\lambda_g$, we can determine the $E_{Opg}$ significant peaks in polar MC and MC/CQD samples from Fig. 13B.[58] For MCQDS0, MCQDS1, and MCQDS2, the computed $E_{Opg}$ values are 4.30 eV, 3.21 eV and 2.49 eV, respectively. The significant electrical interaction between CQDs and the MC polymer matrix is confirmed by the steady drop in $E_{Opg}$ with increasing CQD content. CQDs induce optical properties in the MC matrix and the presence of localized defect states and improved hydrogen bonding resulting from surface functional groups on CQDs are responsible for this decrease. These factors increase structural disorder and promote sub-band-gap optical transitions. Overall, the refractive index is a function of the wavelength, $n = n(\lambda)$. This means that when light hits a substance, different wavelengths ($\lambda$) move through it at different speeds. This is called optical dispersion. The refractive index increases with concentration due to the rise in localized states within the forbidden energy gap, while the phase velocity decreases. This change in the electrical structure changes how the material spreads out, which in turn changes how light travels through it. An optical pulse is made up of multiple monochromatic waves. As it goes across a dispersive medium, each frequency component moves at a distinct speed. This is why the pulse's strong peak gets wider and flatter over time. This shows that the material is absorbing and spreading out the light. Since phase velocity doesn't carry information, it can be faster than the speed of light. In contrast, group velocity cannot exceed the speed of light because information is transmitted by group velocity; the current study confirms this point. In the anomalous dispersion regime, the group velocity may exceed the speed of light; however, this apparent superluminal

behavior does not correspond to superluminal information transfer. Slow light propagation can significantly enhance linear and nonlinear optical effects, enabling applications in photonic devices such as optical delay lines, all-optical signal processing, optical switching, fibers, and optical storage systems.[61,63]

### 3.9. Dielectric study

One of the inherent characteristics of materials is the dielectric property, which is represented by a complex dielectric function ($\varepsilon^*$), and it gauges how materials respond when they come into contact with an electric field that induces polarization.[64] The dielectric constant of materials, as delineated in eqn (6), comprises a real component, $\varepsilon_r$ and an imaginary component, $\varepsilon_i$. The real component signifies the material's ability to attenuate the velocity of light, while the imaginary component indicates its efficacy in energy absorption due to polarisation.[65]

$$\varepsilon^* = \varepsilon_r + i\varepsilon_i \quad (6)$$

$\varepsilon_r$ is derived from the index of refraction ($n$) of the medium ($\varepsilon_r = n^2 - k^2$), while $\varepsilon_i$ is calculated using $k$.[49] Polymer materials designed for energy storage applications must have elevated capacitance density, attainable *via* a high dielectric constant. Recently, considerable efforts have been focused on optimizing the dielectric characteristics of polymer materials to satisfy the specifications for their integration into capacitors and energy storage devices.[64] Fig. 14 illustrates the dielectric spectra ($\varepsilon_r$) of pure MC and MC/CQD NNC films as a function of wavelength, indicating a progressive rise in $\varepsilon_r$ from 1.344 to 2.297 with the incorporation of CQDs into the MC polymer. CQDs induce optical properties in the MC matrix, and improved dielectric response, along with adjustable optical characteristics, validates the use of MC/CQD NNC films for optoelectronic device applications such as solar cells, photodetectors, and photodiodes.[66] Furthermore, the enhancement in $\varepsilon_r$ is attributable to the elevated density of localized charge carriers and interfacial polarization arising from the interaction between CQDs and the polar functional groups of the MC chains. The Spitzer–Fan model posits a high correlation between the $\varepsilon_r$ and the density of electronic states within the $E_{Opg}$ of polymeric materials.[54] Consequently, the observed enhancement in $\varepsilon_r$ with increasing CQD loading indicates a significant rise in the density of localized states within the $E_{Opg}$. These localized states originate from surface defects and functional groups (–OH, –COOH, –C═O, and –$NH_2$) present on the CQDs, which introduce additional energy levels and facilitate charge trapping. As a result, the incorporation of CQDs into the MC polymer enhances dipolar and interfacial polarization, leading to an overall improvement in dielectric response and a modification of the electronic structure of the NNC films.

Fig. 15 illustrates the linearity of the graphs representing the direct correlation between the $\varepsilon_r$ constant and the square of the wavelength within designated intervals, so validating the Spiter–Fan equation.[67]

$$\varepsilon_r = \varepsilon_\infty - \frac{e^2}{4\pi^2 c^2 \varepsilon_0} \times \frac{N}{m^*}\lambda^2 \quad (7)$$

where the effective mass of the electron $m^* = 1.16m_e$, the dielectric constant of free space is $\varepsilon_0$, the electron charge is $e$ and the concentration of charge carriers is $N$. The constant values are presented in Table 2. Thus, eqn (7) can be utilized to estimate the parameters $N/m^*$ and $\varepsilon_\infty$, derived from the analysis of the slopes and intercepts of the $\varepsilon_r$ *vs.* square wavelength graph, as presented in ref. 54. This table indicates that with increasing CQD concentration, the localized density of states in the MC film rises from $26.3836 \times 10^{55}$ to $113.8790 \times 10^{55}$ $m^{-3}$ $kg^{-1}$; additionally, the high-frequency dielectric constant ($\varepsilon_\infty$) increases from 1.3929 to 3.3131. This rising localized density and $\varepsilon_\infty$ can be attributed to the introduction of additional localized electronic states and charge-transfer pathways by the CQDs, as well as to enhanced interfacial polarization at the MC/CQD interfaces.[54]

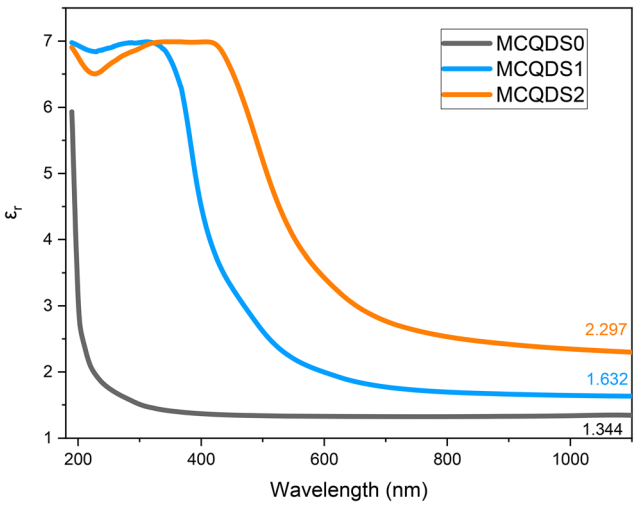


Fig. 14 Real component of the dielectric constant spectra *vs.* wavelength (nm) for both pure and doped MC materials.

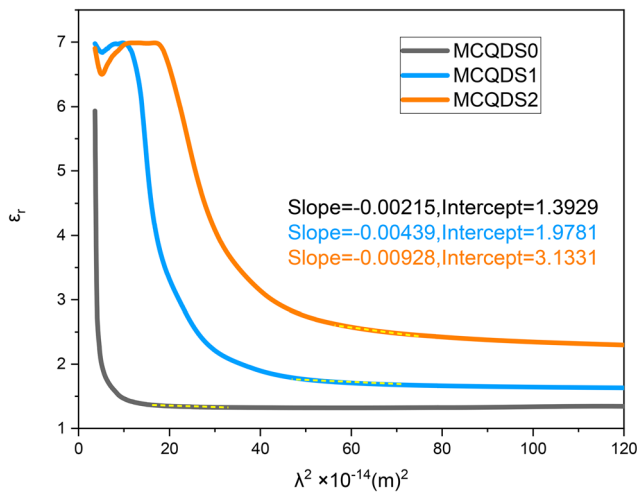


Fig. 15 $\varepsilon_r$ spectral variation for pure and MC:CQD nanocomposites against a double wavelength.

Table 2 Localized density and dielectric constant at short wavelengths (nm) for pure and doped MC samples

| Samples | $N/m^* \times 10^{55}$ ($m^3$ $kg^{-1}$) | $\varepsilon_\infty$ |
|---|---|---|
| MCQAS0 | 26.3836 | 1.3929 |
| MCQAS1 | 53.8716 | 1.9781 |
| MCQAS2 | 113.8790 | 3.1331 |

Fig. 16 shows the change in $\varepsilon_i$ with the triple wavelength for both pristine and MC:CQD nanocomposites films. The relaxation time ($\tau$) can be calculated by inserting the localized density value into eqn (7). Eqn (8) and (9) were used to derive the values for optical mobility ($\mu_{Opt}$) and optical resistivity ($\rho_{Opt}$), which are shown in Table 2.[68]

$$\varepsilon_i = \left(\frac{e^2}{8\pi^3 c^3 \varepsilon_0}\right)\frac{N}{m^*}\left(\frac{1}{\tau}\right)\lambda^3 \quad (8)$$

$$\mu_{Opt} = \frac{e\tau}{m^*} \quad (9)$$

$$\rho_{opt} = \frac{1}{e\mu N_c} \quad (10)$$

$$\omega_{Pl}{}^2 = \frac{e^2 N}{\varepsilon_0 m^*} \quad (11)$$

The comparatively high refractive indices of the MC/CQD NNC films cause a considerable slowdown in light propagation, resulting in reduced values of the optical relaxation time ($\tau$), $\mu_{Opt}$ and $\rho_{Opt}$. The incorporation of CQDs results in an increase in the electron plasma frequency ($\omega_{Pl}$), which rises from $0.87361 \times 10^{15}$ Hz for pure MC to $1.815 \times 10^{15}$ Hz for the CQD-loaded films. The systematic increase in $\omega_{Pl}$ with rise in CQD content can be ascribed to an enhancement in the charge-carrier density ($N$) arising from the introduction of additional localized electronic states and charge-transfer pathways provided by the CQDs. This interpretation is valid under the assumption that the effective mass ($m^*$) of the charge carriers remains approximately constant. Furthermore, strong interfacial interactions between the CQDs and the MC chains promote carrier delocalization, thereby enhancing the composite's overall electronic response. Quantitative evaluation of these optical parameters is essential for understanding light–matter interaction in MC/CQD NNCs and for assessing their potential suitability in optical and optoelectronic device applications.[67] Additionally, robust interactions with the polar MC chains are facilitated by the presence of functional groups such as nitrogen and oxygen on the surface of CQDs, which promotes charge delocalization and improves carrier mobility. The dielectric response of the MC/CQD NNC films is significantly enhanced, illustrating the efficacy of CQDs in modifying the electrical and polarization properties of the polymer system. A significant finding of the present work is the correlation between macroscopic optical properties and microscopic charge-transport behavior. From a macroscopic perspective, an increase in the n leads to a reduction in the $V_P$ propagating through the MC/CQD nanocomposite films. In contrast, from a microscopic viewpoint, a similar trend is observed, as the mobility of charge carriers decreases with increasing CQD concentration. The decline in mobility is due to increased carrier scattering and the emergence of confined states caused by CQDs. Consequently, the persistent reduction in both phase velocity (macroscopic scale) and mobility (microscopic scale) substantiates a robust correlation between the optical response and charge transport pathways in the examined polymer–CQD combination (Table 3).

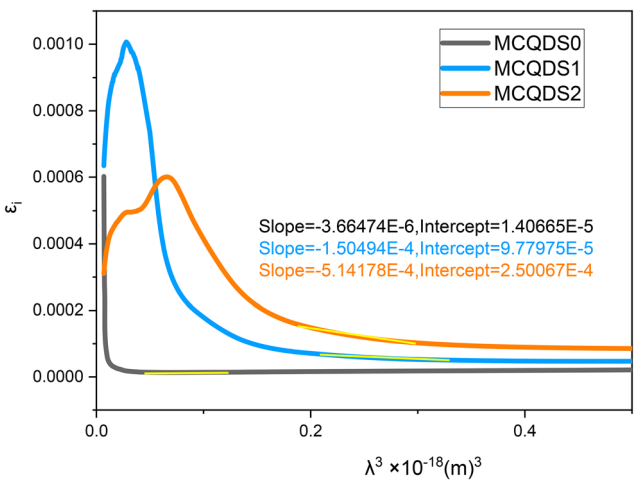


Fig. 16 $\varepsilon_i$ spectral variation for pure MC and MC:CQD nanocomposites against the triple wavelength.

### 3.10. Optical energy gap study

$E_{Opg}$ of semiconductors signifies essential physical characteristics that define their optical and electrical properties. The characteristics and extent of these fundamental material features significantly influence the use of semiconductors in electrical, optical, and optoelectronic devices, thereby facilitating the evaluation of band-gap-designed devices for continuous, optimal absorption of broadband spectral sources. Moreover, devices such as photonic crystals, waveguides, and solar cells[69] rely on the optical band gap energy ($E_{Opg}$), which is defined as the energy range in a material where electronic states are forbidden, a concept widely used in solid-state physics. $E_{Opg}$, situated between the CB and the VB, is a region where electron mobility is restricted. Depending on their energy gap, materials can be categorized as conductors, semiconductors, or insulators. Metals normally display insignificant band gaps, while insulators contain a greater band gap, usually approximately 4.5 eV, in comparison to semiconductors. Materials having significant bandgaps are usually inappropriate for optoelectronic applications.[69] Previous studies have validated that actual $E_{Opg}$ can be ascertained from $\varepsilon_i$ and the characteristics of electron transition have been determined using Tauc's model.[57,70,71] The optical dielectric function theoretically includes all intrinsic effects associated with light–matter interaction processes. Prior research suggests that the primary peak of $\varepsilon_i$ is predominantly affected by electron transitions from the valence band to the conduction band. The imaginary

Table 3 Optical parameters derived from dielectric loss *versus* $\lambda^3$: relaxation time, optical mobility, optical resistivity, and plasma frequency

| Samples | $N/m^* \times 10^{55}$ | $J$ | $\tau \times 10^{-13}$ | $\mu_{opt}$ | $N_c \times 10^{26}$ | $\rho_{opt} \times 10^{-8}$ | $\omega_{Pl} \times 10^{15}$ |
|---|---|---|---|---|---|---|---|
| MCQAS0 | 26.3836 | 114.1091 | 311.37 | 4.7195 | 2.785 | 0.4755 | 0.87361 |
| MCQAS1 | 53.8716 | 232.9948 | 15.482 | 0.2347 | 5.6867 | 4.6835 | 1.2483 |
| MCQAS2 | 113.8790 | 492.5267 | 9.5789 | 0.1452 | 12.021 | 3.581 | 1.815 |

component of the dielectric loss characteristic is analyzed concerning the $h\nu$ capacity for energy gap assessment. The optical properties and electrical band structure are tightly linked. Understanding the real and imaginary components of the dielectric function enables the calculation of critical optical characteristics. The optical polarizability and attenuation of the material relate to the real and imaginary components of the dielectric, respectively. Consequently, photonic dielectric loss is crucial for the precise evaluation of $E_{Opg}$.[71,72]

$$\varepsilon_i = \frac{2\pi e^2}{\Omega \varepsilon_0} \sum_{K,V,C} \left|\Psi_K^C | u, r | \Psi_K^V\right|^2 \delta\left(E_K^C - E_K^V - \hbar\omega\right) \quad (11)$$

where $\omega$ and $\Omega$ denote the incident photon and the crystal volume, respectively, while $\varepsilon_0$ and $e$ denote the vacuum permittivity and electron charge, respectively. The polarization vector of the incident electromagnetic wave is denoted by $u$, whereas the location vector is represented by $r$. The wave functions for the CB and VB at $K$ are denoted as $\Psi_K^V$ and $\Psi_K^C$, respectively. The theoretical formulation of the optical dielectric constant involves a complex frequency-dependent function; consequently, its accurate determination requires substantial computational effort. On the other hand, measuring the dielectric constant experimentally using the imaginary part of the optical dielectric function ($\varepsilon_i$) is rather simple. This macroscopic technique gives a more predictable method for estimating the optical band gap by utilizing the $n$ and $k$ in the computation, as expressed by the relation $\varepsilon_i = 2nk$.[58,73] You can get the actual $E_{Opg}$ by looking at where the linear part of $\varepsilon_i$ crosses the $h\nu$ axis in the spectrum. The strong link between electron–photon interactions and the optical dielectric function, which shows that interband electronic transitions happen in materials, explains this phenomenon. Fig. 17 shows that you can find the real $E_{Opg}$ by using the $\varepsilon_i$, which is found by crossing linear segments of the $\varepsilon_i$ spectra along the horizontal axis of photon energy. This figure indicates that the energy bandgap of pure MC film is 6.1 eV, which then decreases significantly to 2.85 eV for MCQDS1 and 1.9 eV for MCQDS2. Our prior research revealed pronounced peaks in the $\varepsilon_i$ plot, attributable to the amorphous characteristics of the samples. The extensive peaks illustrated in Fig. 17 can be attributed to the amorphous form of the samples.[74] Table 4 presents the estimated $E_{Opg}$ derived from the $\varepsilon_i$ plots. The chart shows that the $E_{Opg}$ drops progressively with increasing CQD content in the MC polymer matrix. It should be noted that the observed reduction in optical band gap corresponds to an effective optical band gap arising from localized states and defect-induced transitions, rather than a true bulk-like band structure modification. This behavior is characteristic of disordered polymer nanocomposites, where

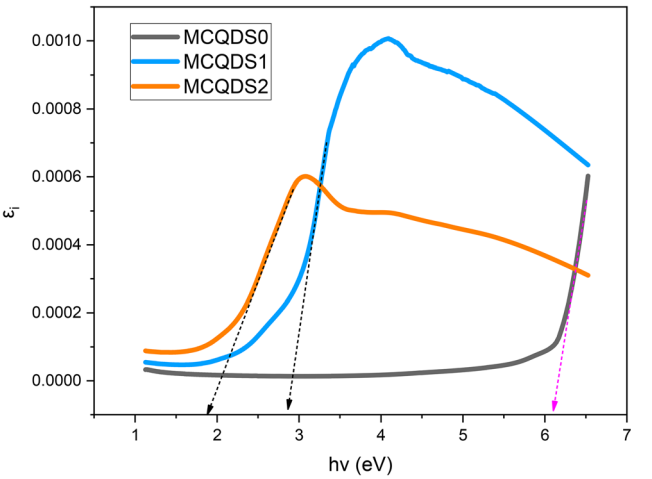


Fig. 17 $\varepsilon_i$ spectral variation for pure MC and MC:CQD nanocomposites against $h\nu$.

Table 4 Correlation of $E_{Opg}$ (eV) from Tauc's model with photon energy $(\alpha h\nu)^{1/T}$ and $\varepsilon_i$

| Samples | $(\alpha h\nu)^2$ | $(\alpha h\nu)^{2/3}$ | $(\alpha h\nu)^{1/2}$ | $(\alpha h\nu)^{1/3}$ | $\varepsilon_i$ |
|---|---|---|---|---|---|
| MCQDS0 | 6.2 | 5.95 | 5.8 | 5.6 | 6.1 |
| MCQDS1 | 2.9 | 2.6 | 2.5 | 2.45 | 2.85 |
| MCQDS2 | 2.7 | 1.8 | 1.45 | 1.4 | 1.9 |

sub-band-gap transitions are governed by tail states and interfacial electronic interactions. The absorption behavior in the low-energy region follows the Urbach rule, $\alpha(h\nu) = \alpha_0 \exp(h\nu/E_U)$, where $E_U$ represents the Urbach energy associated with localized tail states. This trend indicates strong electrical interactions between the CQDs and the polar MC chains, which enhance optical absorption. These interactions arise from the incorporation of CQDs into the host polymer, creating localized charge-carrier states (trapping sites) within the band structure. The presence of these confined states facilitates electronic transitions at lower energies, thereby causing the observed reduction in $E_{Opg}$.[74]

Quantum mechanical principles offer fundamental insight into light–matter interactions and the functioning of electronic materials. However, from a practical and quantitative perspective, Tauc's relation is widely recognized as one of the most accurate methods for evaluating the $E_{Opg}$ in nanocomposite systems. Accurate determination of the $E_{Opg}$ from optical absorption data often necessitates careful consideration of alternative approaches, particularly due to the presence of band-tail states near the VB and CB. Despite these complexities,

Tauc's model remains one of the most effective and commonly employed techniques for determining the $E_{Opg}$.[75]

$$\alpha h\nu = M(h\nu - E_{Opg}) \quad (13)$$

where $M$ represents a constant that is independent of energy. The $E_{Opg}$ can be calculated by utilizing eqn (12) on the recorded UV-vis spectra of the samples. Moreover, the characteristics of the electronic transition can be found by defining the value of $T$. For direct electronic transitions, $T$ takes the values 1/2 or 3/2, while for indirect transitions, $T$ equals 2 or 3, depending on whether the transitions are allowed or forbidden, respectively.[52] In crystalline solids, a direct transition occurs when an electron is promoted from the VB to the CB without a change in crystal momentum, meaning the transition happens at the same point in $k$-space and conserves both energy and momentum. In contrast, an indirect transition involves electronic states at different $k$-space positions within the conduction and valence bands. Such transitions can occur only with the assistance of phonons, which provide the required momentum compensation.[76] By extrapolating the intersection of the linear segment of the $(\alpha h\nu)^{1/T}$ with the $\alpha h\nu$ axis, one can obtain the value of $E_{Opg}$ in Fig. 18. The type of transition can be determined by comparing the $E_{Opg}$ values derived from the dielectric loss plot with those obtained from the Tauc's equation model, as can be seen in Table 4.[45,65] By comparing the $E_{Opg}$ values obtained from Tauc's model (Fig. 18A–D) with the energies derived from $\varepsilon_i$ (Fig. 17), the nature of the electronic transitions can be determined. Specifically, for MCQDS0 and MCQDS2, the transitions are classified as direct forbidden ($T$ = 3/2), whereas for MCQDS1, they are identified as direct allowed ($T$ = 1/2). Moreover, the XRD results validated that the MC crystalline structure was compromised by the CQDs. The mismatch between the VB and the CB is a well-known characteristic of amorphous materials, which prevents direct allowed transitions. Notably, despite structural distortions in the MC:CQD NNC samples, they retain significant crystalline regions, as confirmed by XRD analysis and morphological observations. Consequently, the direct forbidden ($T$ = 2/3) outcomes for composite samples are linked to the diminished crystalline order in the MC:CQD NNC. The $E_{Opg}$ value (generally less than 2) for MC/CQD films renders them appropriate foundational structures for solar cell applications, organic light-emitting diodes (OLEDs),[64] photo-detectors and photovoltaic cells.[50]

Table 5 summarizes the variation in $E_{Opg}$ and $n$ of MC-based nanocomposites as a function of CQD content. The results clearly demonstrate that the incorporation of CQDs causes a significant narrowing of the band gap, indicating strong electronic coupling between the CQDs and the methylcellulose matrix. By comparison, other modifiers such as polymer blends, organic dyes, ceramic fillers, or conventional nanoparticles typically produce only marginal reduction in the $E_{Opg}$.

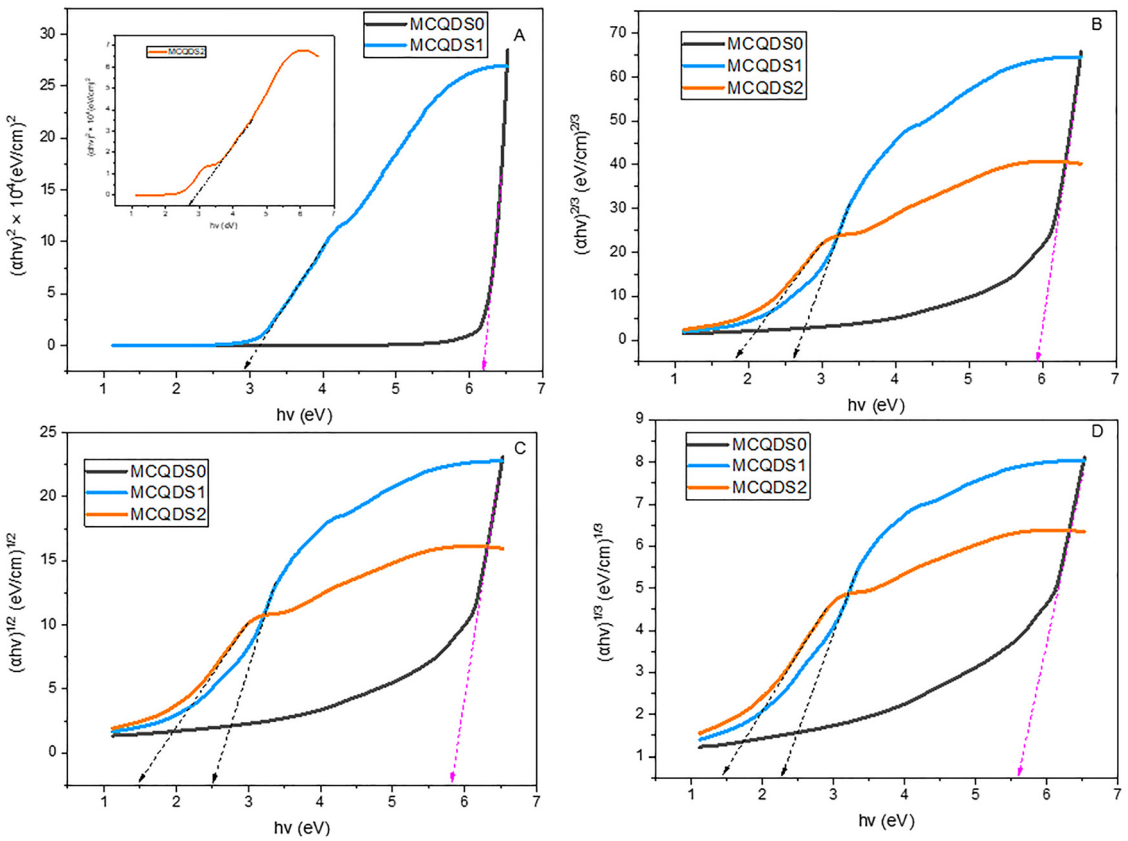


Fig. 18 (A–D) Tauc's spectral plots for different kinds of transitions *versus* $h\nu$.

Table 5 Energy gap and refractive index of the MC polymer NNC with varying concentrations of CQDs and other additives (dye, polymer blends, ceramic fillers, and nanoparticles)

| Doped polymer | $E_{Opg}$ (eV) | $n$ | Ref. |
|---|---|---|---|
| MC:CuS nanoparticles (NPs) | 6.24–2.35 | 1.18–2.06 | 10 |
| MC:hollyhock (HH) dye | 5.6–2.7 | — | 12 |
| MC:$CuCl_2$ salt | 6.21–2.68 | 1.44–2.04 | 13 |
| MC:Ag NPs | 5.76–4.27 | — | 15 |
| CS (chitosan)/MC: $LiBF_4$ | 5.10–4.88 | 2.44–2.63 | 77 |
| MC:Cosmos sulphureus Cav. (CSC) flowers | 6.2–2.3 | 1.15–1.18 | 68 |
| MC:$Pb^{2+}$ | 6.32–4.44 | — | 78 |
| MC:methylene blue | 6.29–5.95 | — | 79 |
| MC:CQDs | 6.1–1.9 | 1.159–1.516 | Present work |

The pronounced influence of CQDs is attributed to the formation of localized charge-carrier states within the polymer network, which act as trapping centers and enable lower-energy electronic transitions. This modification enhances optical absorption, thereby improving the suitability of the composite for optoelectronic applications.

**3.10.1. Cody representations for the bandgap study.** Cody contended that the rising value of Tauc's optical gap, linked to the reduction in film thickness, arises from the curvature of the dependency of the spectra of the function $(\alpha/h\nu)^{1/T}$ on the energy of the input photon. The $E_{Opg}$ of the MC/CQDs films with varying thicknesses can be ascertained from the intersection of the linear segment depicted in the graph of $(\alpha/h\nu)^{1/T}$ *versus* photon energy. The convergence of this linear extension along the abscissa, according to the Cody model of $E_{Opg}$, enables the calculation of $E_{Opg}$, yielding the band energies depicted in Fig. 19(A–D) for the allowed direct and indirect transitions, respectively. Cody representations exhibit a slight curvature in comparison to Tauc's plots and reveal a reduced dependence of the optical gap on the thickness of thin CQD layers, unlike the observations made using Tauc's technique. Tauc asserted that the momentum matrix component is unaffected by $h\nu$, whereas Cody proposed that the dipole matrix element is likewise not reliant on $h\nu$. Table 6 presents the estimated $E_{Opg}$ values derived from Cody's method.[75,80] By juxtaposing the $E_{Opg}$ values derived from the Cody model (Fig. 19A–D) with those acquired from the optical dielectric loss spectra, the characteristics of the electronic transitions may be accurately discerned. The analysis indicates that both MCQDS0 and MCQDS1 demonstrate direct band transitions with a transition index of $T = 3/2$. At the same time, MCQDS2 displays a direct allowed transition with $T = 1/2$, further demonstrating that the insertion of CQDs induces optical properties in the MC matrix and modifies the structure of the MC matrix in a predictable manner, thereby substantiating the validity of the employed optical models. When comparing results from Tauc's plots and Cody's representations, there

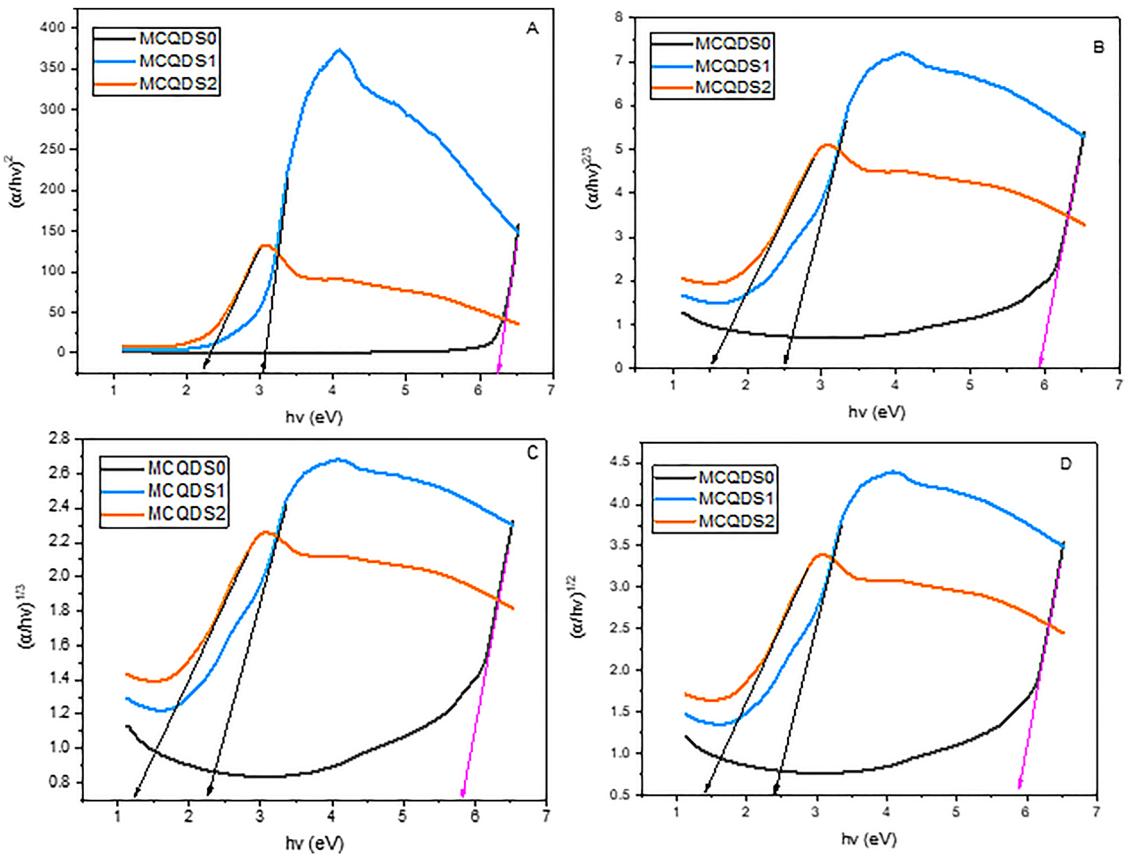


Fig. 19 (A–D) Cody spectral plots for different kinds of transitions *versus* $h\nu$ satisfied Tauc's models.

Table 6 Optical energy gap ($E_{Opg}$) of MC and MC/CQD nanocomposites evaluated using the Cody method from optical absorption data

| Samples | $(\alpha/h\nu)^2$ | $(\alpha/h\alpha)^{2/3}$ | $(\alpha/h\alpha)^{1/2}$ | $(\alpha/h\alpha)^{1/3}$ | $\varepsilon_i$ |
|---|---|---|---|---|---|
| MCQDS0 | 6.25 | 5.95 | 5.9 | 5.8 | 6.1 |
| MCQDS1 | 3.4 | 2.5 | 2.4 | 2.25 | 2.85 |
| MCQDS2 | 2.2 | 1.5 | 1.4 | 1.2 | 1.9 |

are slight variances in $E_{Opg}$ levels that can be ignored when taking the measurement error range into account. It is possible to conclude that these distinctions are not important, making their use unnecessary. The energy band gap for both organic and inorganic semiconductors can be computed using these models.

**3.10.2. Differentiation methods for bandgap estimation.** This study primarily examines the determination of $E_{Opg}$ for permitted direct transitions using various methods. The $E_{Opg}$ is found by many methods, the initial three of which include graphing the first derivative as a function of photon energy for transmittance spectra, refractive index, and reflectance spectra. In these methods, the energy of the gap is determined from the initial maximum apex in the higher-energy range on the *x*-axis (see Fig. 20A–C), where the position of the highest peak correlates with the optical energy gap.[62,81] The analysis of solid

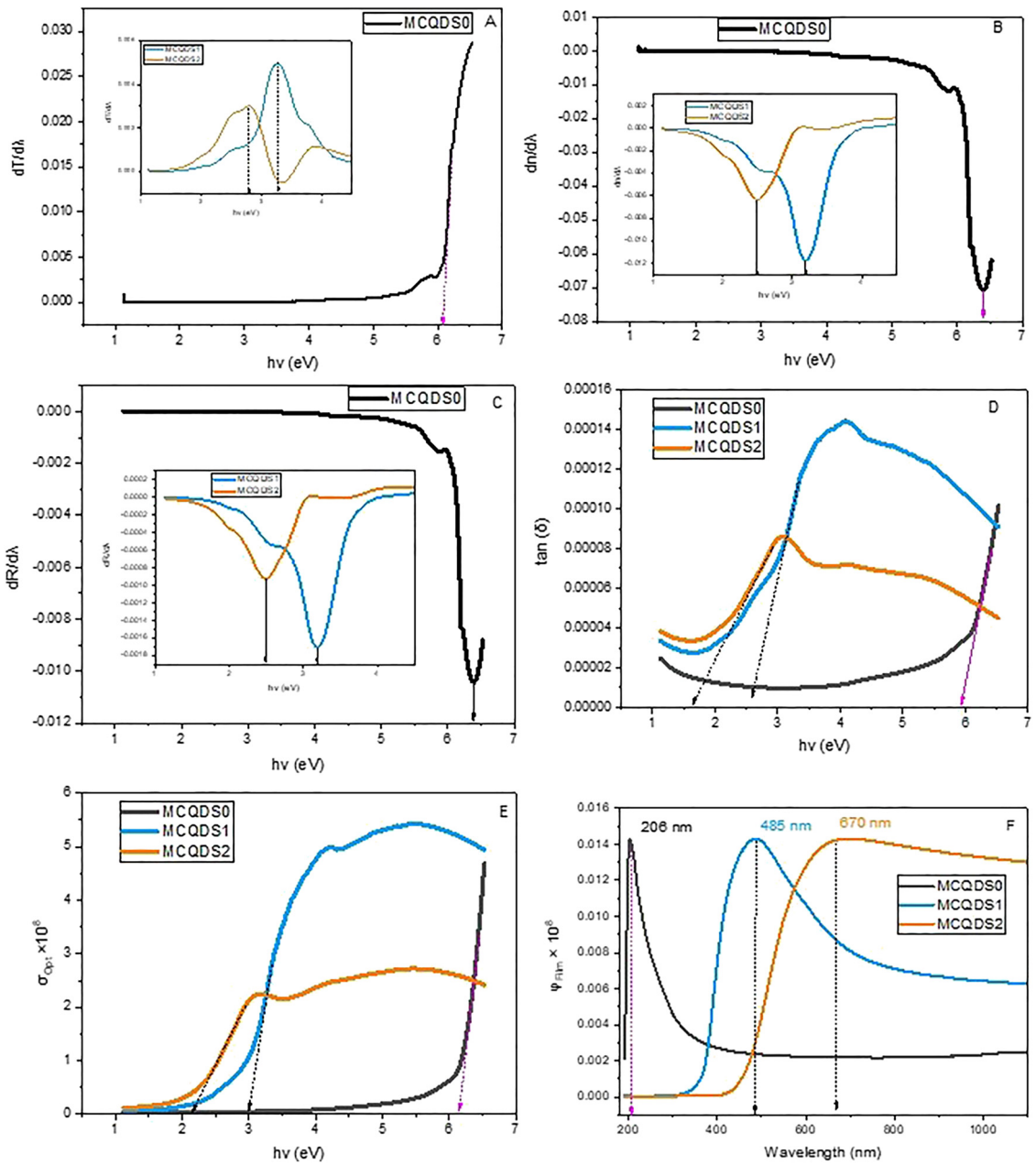


Fig. 20 Various techniques used to determine the optical band gap $E_{Opg}$ of MC and MC/CQD nanocomposite films from the corresponding optical spectra.

structures and defects involves examining the dielectric loss tangent, which is calculated from the measured dielectric constant values. The dielectric parameter ($\tan\delta$) is defined as the ratio of the $\varepsilon_i$ component to the $\varepsilon_r$ of the dielectric constant. Consequently, $\tan\delta$ is defined as:[56]

$$\tan\delta = \frac{\varepsilon_i}{\varepsilon_r} \quad (14)$$

Fig. 20D illustrates the dependency of $\tan\delta$ on $h\nu$ for both pristine MC and MC/CQD nanocomposite films. The $\tan\delta$ demonstrates elevated levels at high $h\nu$ throughout all analyzed samples, corresponding to a rise in CQD concentration. Moreover, a rise in CQDs leads to a decrease in the value of $E_{Opg}$. The last approach is optical conductivity ($\sigma_{opt}$), which possesses the dimension of frequency in the Gaussian system of units, is suitable for optical materials, and is often derived from the $n$ and $\alpha$ values, using the following relation.[82]

$$\sigma_{opt} = nac/4\pi \quad (15)$$

The optical conductivity ($\sigma_{opt}$) of both pristine MC and MC/CQD nanocomposite films was evaluated using the corresponding relation. Fig. 20E depicts the dependence of $\sigma_{opt}$ on photon energy ($h\nu$) for the undoped and CQD-incorporated MC samples. From these plots, it is evident that the logarithmic values of $\sigma_{opt}$ increase approximately linearly with rising photon energy and then exhibit a sharp upturn as the photon energy approaches the $E_{Opg}$ of the materials. This sudden increase in optical conductivity indicates the generation of a large population of free charge carriers resulting from electronic transitions from the valence band to the conduction band within the polymeric electronic structure.[82] Another way to determine the energy band gap is the figure of merit ($\varphi_{film}$) for transparent films, written as $\varphi_{film} = T^{10}/R$, where $R_s$ denotes sheet resistance. The film's $R_s$ measures the electrical resistance $R_s$ of the films. Minimal sheet resistance is crucial for transparent electrodes in technical gadgets and solar cells, since it indicates enhanced electrical conductivity.[83] Consequently, $\varphi_{film}$ has been established to improve the physical properties of MC/CQD films. The merit of the composite samples was progressively enhanced with rising CQD concentration. We can calculate the $E_{Opg}$ from the absorption edge or significant peaks in pure MC polymer and MC/CQD samples by using $E_{Opg} = 1239.83/\lambda$ (see Fig. 20F). The optical bandgap values obtained from all these approaches are compiled in Table 7, which clearly indicates that the energy gap figures are converging across all techniques. The optical bandgap values diminish with increasing concentrations of CQDs. The reduction of the energy gap with the incorporation of CQDs into the MC matrix indicates the emergence of disorder within the polymer structures, resulting in the creation of localized energy states within the forbidden energy band gap. This phenomenon leads to the formation of trap levels during the transition from the HOMO to the LUMO in the MC/CQDs, thereby decreasing the energy required for the electron transition.[56] It is obvious through comparing five differentiation approaches for band gap analysis across all composite samples with dielectric loss that $dT/d\lambda$ is a notable strategy for MCQDS0, $\sigma_{opt}$ is prominent for MCQDS1, and $\varphi_{film}$ is exceptional for MCQDS2.

Table 7 Various techniques for examining the optical band gap $E_{Opg}$ and contrasting it with hypothetical dielectric loss

| Samples | $dT/d\lambda$ | $dR/d\lambda$ | $dn/d\lambda$ | $\sigma_{opt}$ | $\tan\delta$ | $\varphi_{film}$ | $\varepsilon_i$ |
|---|---|---|---|---|---|---|---|
| MCQDS0 | 6.1 | 6.39 | 6.39 | 6.15 | 5.9 | 6.02 | 6.1 |
| MCQDS1 | 3.28 | 3.17 | 3.18 | 3 | 2.55 | 2.56 | 2.85 |
| MCQDS2 | 2.79 | 2.48 | 2.49 | 2.15 | 1.6 | 1.85 | 1.9 |

**3.10.3. Wemple and DiDomenico (WDD) method.** Wemple and DiDomenico (WDD) formulated the concept of a single-oscillator model for the electronic dielectric constant. The model is applicable for characterizing refractive index dispersion at photon energies beneath the interband absorption threshold. In the single-oscillator model, the frequency-dependent dielectric constant is employed to delineate two energy quantities, $E_0$ and $E_d$.

$$\frac{1}{n^2-1} = -\frac{1}{E_0E_d}(h\nu)^2 + \frac{E_0}{E_d} \quad (16)$$

$$n_0 = -\sqrt{1+\frac{E_d}{E_0}} \quad (17)$$

Location of oscillator energy ($E_0$) represents the average excitation energy for electronic transitions, while ($E_d$) is the dispersion energy, which quantifies the average strength of interband optical transitions.[84] Moreover, $E_d$ links the coordination number and the charge distribution within each unit cell, which is intrinsically associated with chemical bonding.[85] The values of ($E_d$) and ($E_0$) can be derived from the intercept and slope of the fitted lines in the graph of $\frac{1}{n^2-1}$ against square phone energy, as illustrated in Fig. 21. The WDD dispersion parameters, $E_0$ and $E_d$, for all films were directly derived from the slope $(E_0E_d)^{-1}$ and the intercept $(E_0/E_d)$ of the linear equations, as

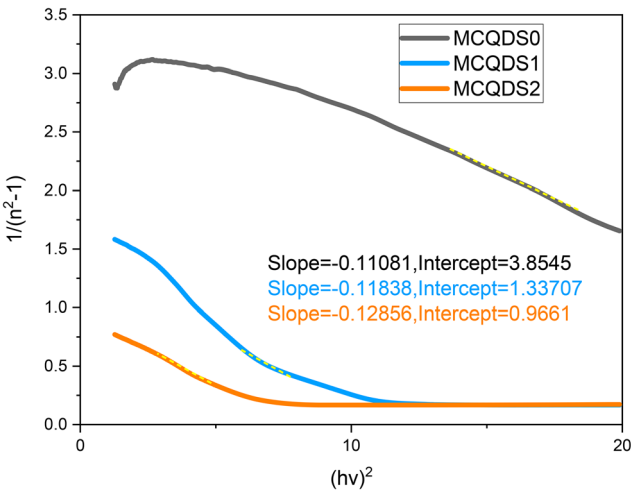


Fig. 21 WDD spectral analysis of MC and MC/CQD nanocomposites showing the variation of $1/(n^2-1)$ as a function of $(h\nu)^2$.

Table 8 Optical dispersion and nonlinear optical parameters of MC and MC/CQD nanocomposites obtained using the WDD single-oscillator model

| Samples | $E_d$ | $E_0$ | $n_0$ | $\chi_1$ | $\chi_1 \times 10^{-17}$ | $n_2 \times 10^{-16}$ | $f$ |
|---|---|---|---|---|---|---|---|
| MCQDS0 | 1.5301 | 5.8979 | 1.2594 | 0.2037 | 3.08967 | 9.2437 | 9.0245 |
| MCQDS1 | 2.5135 | 3.3608 | 1.7479 | 0.5871 | 213.387 | 460.003 | 8.4474 |
| MCQDS2 | 2.8375 | 2.7413 | 2.0351 | 0.8125 | 782.882 | 1449.52 | 7.7785 |

presented in Table 8. It is evident that augmenting the concentration of CQDs resulted in a reduction of the single $E_0$ and an elevation of $E_d$. This model proposes that $E_0$ is correlated with the optical band gap ($E_{Opg}$).[86] For the present films, the $E_0$ values were nearly equal to the corresponding $E_{Opg}$ values (see Table 8). Moreover, dispersion plays a critical role in the study of optical materials, serving as a fundamental parameter in optical communication and device design. The static refractive index values $n_0$ (the zero-frequency refractive index) of the analyzed films were derived from the WDD dispersion parameters $E_0$ and $E_d$ utilizing eqn (17),[86] which improves the material's strength. The rise in the value of $n_0$ correlates with improved polarizability. Systems like CQDs may perturb the lattice structure, resulting in a reduction in lattice energy and an elevation in the value of $n_0$.[87] The strength of an individual oscillator ($f$) is defined as $f = E_0E_d$, refer to Table 8. The field of nonlinear optics is expected to enable a wide range of photonic devices. This motivates the investigation of the nonlinear optical properties of MC-CQD NNCs at different concentrations. Accordingly, the linear optical susceptibility ($\chi^{(1)}$) and the third-order nonlinear optical susceptibility ($\chi^{(3)}$) of the MC-CQD composites have been determined for the nonlinear optical analysis

$$\chi^{(1)} = \frac{E_d/E_0}{4\pi}, \chi^{(3)} = 6.82 \times 10^{-15}(E_d/E_0)^4 \quad (18)$$

Table 8 presents the values of $\chi^{(1)}$ and $\chi^{(3)}$, which exhibit a progressive increase corresponding to the rising content of CQDs. Moreover, the determination of the nonlinear refractive index is crucial for numerous optoelectronic applications; consequently, the nonlinear refractive index ($n_2$) for the MC-CQD NNC is determined using $\chi^{(3)}$ and $n_0$ data, using the following equation.

$$n_2 = 12\pi\chi^{(3)}/n_0 \quad (19)$$

The estimated values of $n_2$ improve with the addition of CQDs, as shown in Table 8. Because of their unusual optical properties, MC-CQDs lead the field in optoelectronic applications.[88] In addition, at higher CQD loadings, quantum confinement effects become increasingly significant, leading to the formation of additional discrete energy levels and the amplification of nonlinear optical phenomena. The observed enhancement in third-order nonlinear oscillatory behavior is primarily attributed to the increased density of electronic states near the band edges. Furthermore, the reduction in the optical band gap ($E_{Opg}$) enables electronic transitions at lower photon energies, thereby facilitating multiphoton excitation within the composite system. Owing to the pronounced improvement in nonlinear optical parameters, most notably the substantial increase in third-order nonlinear susceptibility ($\chi^{(3)}$) and nonlinear refractive index ($n_2$), the MC/CQD nanocomposite films developed in this study exhibit strong potential for advanced photonic and optoelectronic applications. Such materials are particularly suitable for all-optical switching, optical limiting, and modulation devices that require media with high nonlinear optical response.[87]

## 4. Conclusion

In this study, CQDs were sustainably synthesized from the coffee residue using a hydrothermal method. HRTEM, XRD, and structural and morphological evaluations verified the synthesis of ultrasmall CQDs with particle sizes below 5 nm and primarily amorphous properties. XPS and FTIR surface chemistry analyses revealed the presence of several functional groups, including –OH, –NH, C═O, C–N, and C═C. These groups are crucial for enhancing the functionality of the methylcellulose (MC) polymer matrix in conjunction with other components. The incorporation of CQDs into MC enhanced the optical characteristics of the MC polymer. The UV-visible absorption spectrum shows that the MC/CQD nanocomposite improves light absorption, significantly reducing the optical gap from 6.1 eV (MCQDS0) to 1.9 eV (MCQDS2). This was validated by Tauc's plot, $\tan\delta$, $\sigma_{opt}$, $\varphi_{film}$, and the differentiation method. The heteroatoms and functional groups (C═O, $NH_2$, and COOH) in CQDs are thought to have reduced the energy gap by creating localized energy states, and better optically inferred interfacial electronic interactions have led to an increased Urbach tail. The refractive index rises from 1.15 to 1.51, indicating an increase in the number of charge carriers and the composite system's polarization capacity, which is suitable for optoelectronic devices. Studies of photoluminescence show that our CQDs have a quantum yield of 4.55%. This means that they would work well in optoelectronic devices. The emergence and alteration of unique peaks in the group velocity spectra demonstrated that CQDs can modify light propagation and reduce photon velocity within the MC polymer. The study, which employed optical dielectric functions and the Wemple-DiDomenico model, augmented our understanding of the dispersion properties and fundamental optoelectronic features of the nanocomposites. This study shows that use of natural CQDs is an efficient, cost-effective, and environmentally friendly method for inducing the optical properties of MC polymers. The MC–CQD nanocomposites are a great candidate for applications in photoelectronic devices.

## Conflicts of interest

The authors confirm that they have no known competing financial interests or personal relationships that could have appeared to influence the work reported in this paper.

## Data availability

The data supporting the findings of this study are available from the corresponding author upon reasonable request. All relevant data generated or analyzed during this study are included in this published article.

## Acknowledgements

The authors gratefully acknowledge the financial support for this study from the University of Sulaimani, Charmo University, University of Raparin and United Arab Emirates University. The authors acknowledge the UAEU-AUA joint research program under the grant number 12R248 and the National Water and Energy Centre, United Arab Emirates University, U.A.E., for financial support.

## References

1 Z. A. Qureshi, *et al.*, Carbon dots as versatile nanomaterials in sensing and imaging: efficiency and beyond, *Heliyon*, 2024, **10**(11), e31634.
2 M. E. Khan, A. Mohammad and T. Yoon, State-of-the-art developments in carbon quantum dots (CQDs): photocatalysis, bio-imaging, and bio-sensing applications, *Chemosphere*, 2022, **302**, 134815.
3 P. K. Yadav, *et al.*, Carbon quantum dots: synthesis, structure, properties, and catalytic applications for organic synthesis, *Catalysts*, 2023, **13**(2), 422.
4 S. Das, S. Mondal and D. Ghosh, Carbon quantum dots in bioimaging and biomedicines, *Front. Bioeng. Biotechnol.*, 2024, **11**, 1333752.
5 X. Xu, *et al.*, Hydrothermal synthesis of biomass-derived CQDs: advances and applications, *Nanotechnol. Rev.*, 2025, **14**(1), 20250184.
6 S. Chahal, *et al.*, Green synthesis of carbon dots and their applications, *RSC Adv.*, 2021, **11**(41), 25354–25363.
7 S. Ahmad, *et al.*, *Introduction to Green Carbon Dots, in Green Carbon Dots: Sustainable Analytical Approaches*, ACS Publications, 2025, pp. 1–26.
8 N. A. Pechnikova, *et al.*, Carbon quantum dots in biomedical applications: advances, challenges, and future prospects, *Aggregate*, 2025, **6**(3), e707.
9 M. Tavan, *et al.*, Carbon quantum dots: multifunctional fluorescent nanomaterials for sustainable advances in biomedicine and agriculture, *Ind. Crops Prod.*, 2025, **231**, 121207.
10 S. B. Aziz, M. A. Rasheed and H. M. Ahmed, Synthesis of polymer nanocomposites based on [methyl cellulose]$_{(1-x)}$:(CuS)$x$ ($0.02\ \mathrm{M} \leq x \leq 0.08\ \mathrm{M}$) with desired optical band gaps, *Polymers*, 2017, **9**(6), 194.
11 F. H. Alkallas, *et al.*, Methyl cellulose/amorphous $TiO_2$ biodegradable UV-protective films: an investigation into the impact of annealing on their optical properties, *Opt. Mater.*, 2025, 117203.
12 S. B. Aziz, *et al.*, Green chemistry approach to decline the optical band gap of MC polymer using hollyhock natural dye, *J. Inorg. Organomet. Polym. Mater.*, 2025, **35**(3), 2109–2125.
13 A. T. Dana, Effect of $CuCl_2$ powder on the optical characterization of Methylcellulose (MC) polymer composite, *Alexandria Eng. J.*, 2022, **61**(3), 2354–2365.
14 O. G. Abdullah, R. R. Hanna and Y. A. Salman, Structural, optical, and electrical characterization of chitosan: methylcellulose polymer blends based film, *J. Mater. Sci.: Mater. Electron.*, 2017, **28**(14), 10283–10294.
15 A. Atta, *et al.*, Flexible methyl cellulose/polyaniline/silver composite films with enhanced linear and nonlinear optical properties, *Polymers*, 2021, **13**(8), 1225.
16 V. Kansay, *et al.*, Sustainable synthesis of nitrogen-doped fluorescent carbon quantum dots derived from *Cissus quadrangularis* for biomarker applications, *Mater. Chem. Phys.*, 2023, **296**, 127237.
17 R. Atchudan, *et al.*, Sustainable synthesis of carbon quantum dots from banana peel waste using hydrothermal process for *in vivo* bioimaging, *Phys. E*, 2021, **126**, 114417.
18 X. Zhao, *et al.*, Experimental evaluation of detecting power transformer internal faults using FRA polar plot and texture analysis, *Int. J. Electric. Power Energy Syst.*, 2019, **108**, 1–8.
19 G. Ganesh, I. I. Misnon and R. Jose, Solvothermal synthesis of green fluorescent carbon dots from palm kernel shells. *Materials Today: Proceedings*, 2023.
20 G. M. Alshammari, *et al.*, Development of luminescence carbon quantum dots for metal ions detection and photocatalytic degradation of organic dyes from aqueous media, *Environ. Res.*, 2023, **226**, 115661.
21 F. S. Parker, *Porphyrins and related compounds, in applications of infrared spectroscopy in biochemistry, Biology, and Medicine*, Springer, 1971, pp. 350–363.
22 Q. Li, *et al.*, Rac1 activates non-oxidative pentose phosphate pathway to induce chemoresistance of breast cancer, *Nat. Commun.*, 2020, **11**(1), 1456.
23 Q. Xu, *et al.*, Preparation of highly photoluminescent sulfur-doped carbon dots for Fe(III) detection, *J. Mater. Chem. A*, 2015, **3**(2), 542–546.
24 L. Calvo, *et al.*, Effects of support surface composition on the activity and selectivity of Pd/C catalysts in aqueous-phase hydrodechlorination reactions, *Ind. Eng. Chem. Res.*, 2005, **44**(17), 6661–6667.
25 K. K. R. Datta, *et al.*, Yellow emitting carbon dots with superior colloidal, thermal, and photochemical stabilities, *J. Mater. Chem. C*, 2016, **4**(41), 9798–9803.
26 Y. Ran Park, *et al.*, Surface electronic structure of nitrogen-doped semiconducting single-walled carbon nanotube networks, *J. Appl. Phys.*, 2013, **114**(15), 153516.

27 A. Křepelová, *et al.*, The nature of nitrate at the ice surface studied by XPS and NEXAFS, *Phys. Chem. Chem. Phys.*, 2010, **12**(31), 8870–8880.
28 S. Y. Park, *et al.*, Photoluminescent green carbon nanodots from food-waste-derived sources: large-scale synthesis, properties, and biomedical applications, *ACS Appl. Mater. Interfaces*, 2014, **6**(5), 3365–3370.
29 Y. Hu, *et al.*, Waste frying oil as a precursor for one-step synthesis of sulfur-doped carbon dots with pH-sensitive photoluminescence, *Carbon*, 2014, **77**, 775–782.
30 X. Qin, *et al.*, Green, low-cost synthesis of photoluminescent carbon dots by hydrothermal treatment of willow bark and their application as an effective photocatalyst for fabricating Au nanoparticles-reduced graphene oxide nanocomposites for glucose detection, *Catal. Sci. Technol.*, 2013, **3**(4), 1027–1035.
31 S. Liu, *et al.*, Hydrothermal treatment of grass: a low-cost, green route to nitrogen-doped, carbon-rich, photoluminescent polymer nanodots as an effective fluorescent sensing platform for label-free detection of Cu(II) ions, *Adv. Mater.*, 2012, **24**(15), 2037.
32 W. Lu, *et al.*, Economical, green synthesis of fluorescent carbon nanoparticles and their use as probes for sensitive and selective detection of mercury(II) ions, *Anal. Chem.*, 2012, **84**(12), 5351–5357.
33 A. Prasannan and T. Imae, One-pot synthesis of fluorescent carbon dots from orange waste peels, *Ind. Eng. Chem. Res.*, 2013, **52**(44), 15673–15678.
34 Q. Liang, *et al.*, Easy synthesis of highly fluorescent carbon quantum dots from gelatin and their luminescent properties and applications, *Carbon*, 2013, **60**, 421–428.
35 E. Arroyo, *et al.*, Carbon quantum dot optical properties for potential infiltration into hollow core photonic crystal fibers, *Part. Part. Syst. Charact.*, 2023, **40**(6), 2200200.
36 W. Fawaz, J. Hasian and I. Alghoraibi, Synthesis and physicochemical characterization of carbon quantum dots produced from folic acid, *Sci. Rep.*, 2023, **13**(1), 18641.
37 W. Guo, *et al.*, Aromatic C–C bond cleavage in a curved π-system of aminocorannulene, *Org. Lett.*, 2023, **25**(21), 3972–3977.
38 J. Koliyoor, *et al.*, Novel solid biopolymer electrolyte based on methyl cellulose with enhanced ion transport properties, *J. Appl. Polym. Sci.*, 2022, **139**(12), 51826.
39 S. B. Aziz, *et al.*, Structural, electrical and electrochemical properties of glycerolized biopolymers based on chitosan (Cs): Methylcellulose (mc) for energy storage application, *Polymers*, 2021, **13**(8), 1183.
40 R. S. Dassanayake, S. Acharya and N. Abidi, Biopolymer-based materials from polysaccharides: Properties, processing, characterization and sorption applications, in *Advanced sorption process applications*, IntechOpen, 2018.
41 F. He, *et al.*, Hydrogen bond interactions within OH-CQDs/fiber-like carbon nitride for enhanced photodegradation and hydrogen evolution, *Appl. Surf. Sci.*, 2019, **495**, 143558.
42 D. M. Aziz, *et al.*, Spectroscopic study of wemple-didomenico empirical formula and taucs model to determine the optical band gap of dye-doped polymer based on chitosan: common poppy dye as a novel approach to reduce the optical band gap of biopolymer, *Spectrochim. Acta, Part A*, 2025, **325**, 125142.
43 A. Kumar, D. Kumar and M. Saikia, A review on plant derived carbon quantum dots for bio-imaging, *Mater. Adv.*, 2023, **4**(18), 3951–3966.
44 K. R. Ali, *et al.*, Carbon quantum dot derived from the extracted natural dye of hybrid poplar waste leafs as an original progress to enhance the optical properties of PVA polymer: solvothermal synthesis and spectroscopic characterization, *J. Sci.: Adv. Mater. Devices*, 2025, **10**(10100), 9.
45 M. Brza, *et al.*, Tea from the drinking to the synthesis of metal complexes and fabrication of PVA based polymer composites with controlled optical band gap, *Sci. Rep.*, 2020, **10**(1), 18108.
46 A. Edukondalu, *et al.*, Optical properties of amorphous $Li_2O$–$WO_3$–$B_2O_3$ thin films deposited by electron beam evaporation, *J. Taibah Univ. Sci.*, 2016, **10**(3), 363–368.
47 S. B. Aziz, *et al.*, Structural and optical characteristics of PVA: C-dot composites: tuning the absorption of ultra violet (UV) region, *Nanomaterials*, 2019, **9**(2), 216.
48 S. B. Aziz, *et al.*, Optical properties of pure and doped PVA: PEO based solid polymer blend electrolytes: two methods for band gap study, *J. Mater. Sci.: Mater. Electron.*, 2017, **28**(10), 7473–7479.
49 S. B. Aziz, Modifying poly (vinyl alcohol)(PVA) from insulator to small-bandgap polymer: a novel approach for organic solar cells and optoelectronic devices, *J. Electron. Mater.*, 2016, **45**(1), 736–745.
50 S. B. Aziz, *et al.*, From insulating PMMA polymer to conjugated double bond behavior: green chemistry as a novel approach to fabricate small band gap polymers, *Polymers*, 2017, **9**(11), 626.
51 S. Prasher, M. Kumar and S. Singh, Electrical and optical properties of O6+ ion beam-irradiated polymers, *Int. J. Polym. Anal. Charact.*, 2014, **19**(3), 204–211.
52 C. Li, *Refractive index engineering and optical properties enhancement by polymer nanocomposites*, 2016.
53 K. Asai, *et al.*, Synthesis of silyl-functionalized oligothiophene-based polymers with bright blue light-emission and high refractive index, *J. Organomet. Chem.*, 2011, **696**(6), 1236–1243.
54 K. K. Ahmed, S. A. Hussen and S. B. Aziz, Transferring the wide band gap chitosan: POZ-based polymer blends to small optical energy band gap polymer composites through the inclusion of green synthesized Zn2 + -PPL metal complex, *Arabian J. Chem.*, 2022, **15**(7), 103913.
55 S. B. Aziz, *et al.*, Optical properties of pure and doped PVA: PEO based solid polymer blend electrolytes: two methods for band gap study, *J. Mater. Sci.: Mater. Electron.*, 2017, **28**, 7473–7479.
56 D. S. Muhammad, D. M. Aziz and S. B. Aziz, Green tea dye ligands to transfer toxic lead metal ions to precipitated metal complexes for polymer composite applications, *Sci. Rep.*, 2025, **15**(1), 26958.

57 S. B. Aziz, *et al.*, Innovative green chemistry approach to synthesis of $Sn^{2+}$-metal complex and design of polymer composites with small optical band gaps, *Molecules*, 2022, **27**(6), 1965.
58 H. A. Mohammed, P. A. Mohammed and S. B. Aziz, Physical characteristics of polymer composites based on PVA doped with $Mn^{2+}$ metal complexes synthesized by green approach: insights to linear and optoelectronic optical properties, *Oxford Open Mater. Sci.*, 2025, **5**(1), itaf003.
59 S. B. Aziz, *et al.*, Synthesis of PVA/$CeO_2$ based nanocomposites with tuned refractive index and reduced absorption edge: structural and optical studies, *Materials*, 2021, **14**(6), 1570.
60 S. B. Aziz, *et al.*, Optical characteristics of polystyrene based solid polymer composites: effect of metallic copper powder, *Int. J. Met.*, 2013, **2013**(1), 123657.
61 Y. A. Vlasov, *et al.*, Active control of slow light on a chip with photonic crystal waveguides, *Nature*, 2005, **438**(7064), 65–69.
62 A. Qasem, *et al.*, Effective role of cadmium doping in controlling the linear and non-linear optical properties of non-crystalline Cd–Se–S thin films, *J. Mater. Sci.: Mater. Electron.*, 2022, **33**(4), 1953–1965.
63 T. F. Krauss, Slow light in photonic crystal waveguides, *J. Phys. D: Appl. Phys.*, 2007, **40**(9), 2666–2670.
64 S. B. Aziz, *et al.*, A comprehensive review on optical properties of polymer electrolytes and composites, *Materials*, 2020, **13**(17), 3675.
65 D. Q. Muheddin, S. B. Aziz and P. A. Mohammed, Variation in the optical properties of PEO-based composites via a green metal complex: macroscopic measurements to explain microscopic quantum transport from the valence band to the conduction band, *Polymers*, 2023, **15**(3), 771.
66 C. Howlader, *et al.*, Determining the refractive index and the dielectric constant of PPDT2FBT thin film using spectroscopic ellipsometry, *Opt. Mater.ss*, 2020, **110**, 110445.
67 D. S. Muhammad, D. M. Aziz and S. B. Aziz, Zinc metal complexes synthesized by a green method as a new approach to alter the structural and optical characteristics of PVA: new field for polymer composite fabrication with controlled optical band gap, *RSC Adv.*, 2024, **14**(36), 26362–26387.
68 H. A. Mohammed, *et al.*, Investigation of structural and optoelectronic properties in dye-doped MC biopolymer films, *J. Sci.: Adv. Mater. Devices*, 2025, 100968.
69 T. Y. Ahmed, S. B. Aziz and E. M. Dannoun, Role of outer shell electron-nuclear distant of transition metal atoms (TMA) on band gap reduction and optical properties of $TiO_2$ semiconductor, *Res. Eng.*, 2024, **23**, 102479.
70 M. Brza, *et al.*, From green remediation to polymer hybrid fabrication with improved optical band gaps, *Int. J. Mol. Sci.*, 2019, **20**(16), 3910.
71 D. M. Mamand, *et al.*, Green synthesized metal complex as a novel approach to replace conventional ceramic fillers for polymer composite fabrication with desired optoelectronic properties: study of electron interband transition using UV-vis spectroscopic approach, *Emergent Mater.*, 2025, 1–25.
72 C. Bouzidi, *et al.*, Synthesis, characterization and DFT calculations of electronic and optical properties of $CaMoO_4$, *Phys. B: Condens. Matter*, 2016, **497**, 34–38.
73 S. B. Aziz, O. G. Abdullah and M. A. Rasheed, A novel polymer composite with a small optical band gap: new approaches for photonics and optoelectronics, *J. Appl. Polym. Sci.*, 2017, **134**(21), DOI: 10.1002/app.44847.
74 S. B. Aziz, Morphological and optical characteristics of chitosan $(1-x)$: $Cuo_x$ $(4 \leq x \leq 12)$ based polymer nanocomposites: optical dielectric loss as an alternative method for tauc's model, *Nanomaterials*, 2017, **7**(12), 444.
75 H. A. Mohammed, P. A. Mohammed and S. B. Aziz, Investigation of optical band gap in PEO-based polymer composites doped with green-synthesized metal complexes using various models, *RSC Adv.*, 2025, **15**(29), 23319–23341.
76 A. N. Alias, Z. M. Zabidi, A. M. M. Ali and M. K. Harun, Optical characterization and properties of polymeric materials for optoelectronic and photonic applications, *Int. J. Appl. Sci. Technol.*, 2013, **3**(5), 11–38.
77 O. G. Abdullah, *et al.*, Characterization of lithium ion-conducting blend biopolymer electrolyte based on CH-MC doped with LiBF4, *J. Inorg. Organomet. Polym. Mater.*, 2018, **28**(4), 1432–1438.
78 O. G. Abdullah, S. B. Aziz and D. R. Saber, Characterization of pure and $Pb^{2+}$ ion doped methylcellulose based biopolymer electrolyte films: optical and electrical properties, *Int. J. Electrochem. Sci.*, 2018, **13**(12), 11931–11952.
79 O. G. Abdullah, *et al.*, Linear and nonlinear optical characterization of dye–polymer composite films based on methylcellulose incorporated with varying content of methylene blue, *J. Electron. Mater.*, 2022, 1–9.
80 A. S. Hassanien, A. A. Akl and I. M. El Radaf, Comparative studies for determining the optical band-gap energy of the novel polycrystalline thin $ZnGa_2S_4$ films sprayed at different film thicknesses, *Res. Sq.*, 2021, https://api.semanticscholar.org/CorpusID:236750407.
81 V. Dalouji, *et al.*, The optical properties of aluminum-doped zinc oxide thin films (AZO): new methods for estimating gap states, *J. Supercond. Novel Magnet.*, 2019, **32**(5), 1319–1326.
82 P. Dhatarwal and R. Sengwa, Investigation on the optical properties of (PVP/PVA)/Al2O3 nanocomposite films for green disposable optoelectronics, *Phys. B: Condens. Matter*, 2021, **613**, 412989.
83 D. S. Muhammad, D. M. Aziz and S. B. Aziz, The impact of green chemistry to synthesize PVA/cobalt metal complexes (CoMCs) composites with enhanced optical behavior, *Opt. Mater.*, 2025, **158**, 116448.
84 S. N. Kasarova and N. G. Sultanova, Thermal variations of refractive and dispersive parameters of optical polymers, *J. Phys.: Conf. Ser.*, 2021, **1762**, 012004.
85 R. T. Abdulwahid, *et al.*, The study of structural and optical properties of PVA: $PbO_2$ based solid polymer nanocomposites, *J. Mater. Sci.: Mater. Electron.*, 2016, **27**(11), 12112–12118.
86 A. Gupta, K. Malik and R. Kumar, Optical constants of the as-prepared and annealed $(Se_{80}Te_{20})_{94}Ag_6$/PMMA thin films, *Chalcogenide Lett.*, 2021, **18**(9), 549–556.
87 S. Alhassan, *et al.*, Preparation and optical properties of PVDF-$CaFe_2O_4$ polymer nanocomposite films, *Polymers*, 2023, **15**(9), 2232.